J. Fluid Mech. (1986), *vol.* 164, *pp.* 237–273
Printed in Great Britain

Melt motion in a Czochralski crystal puller with an axial magnetic field: isothermal motion

By L. N. HJELLMING AND J. S. WALKER
Department of Theoretical and Applied Mechanics, University of Illinois,
Urbana, IL 61801, USA

(Received 22 January 1985 and in revised form 25 September 1985)

A magnetic field suppresses turbulence and thermal convection in a Czochralski crystal puller. The amounts and distributions of dopants and oxygen in the crystal are determined by the motion of the molten silicon during crystal growth. This paper presents analytical solutions for the melt motion in a Czochralski puller with a strong, uniform, axial magnetic field. The relatively small electrical conductivity of the crystal plays a key role in determining the flow. Certain combinations of crystal and crucible rotation rates lead to flow patterns with a large volume of almost stagnant fluid under most of the crystal face. The values of these rotation rates depend on the magnetic field strength.

1. Introduction

Much of the dislocation-free single-crystal silicon used in electronics is grown by the Czochralski process. Pure polycrystalline silicon is placed in a quartz crucible and is melted by graphite heaters placed around the crucible. The crystal growth is initiated by touching a single-crystal seed to the middle of the melt surface (see figure 1). Dopants are added to the melt to give the crystal particular electrical properties, while oxygen and small quantities of other contaminants enter the melt because the molten silicon slowly dissolves the inside surface of the quartz crucible. The dopants, oxygen and other contaminants either evaporate from the free surface of the melt or enter the crystal. Zulehner (1983) states that 'less than 1 % of the reacting oxygen arrives in the crystal and more than 99 % of the oxygen evaporates out of the melt in the form of SiO'. The crystal puller is swept by a downward flow of argon to carry the SiO from the free surface and any CO from the heaters away from the crystal. The crystal is grown until the crucible is almost empty, and a crystal with a diameter of 8 cm and a length of 1 m can be grown in approximately 12 hours.

One objective is to have controllable, uniform concentrations of dopants, oxygen and other contaminants in the crystal. Oxygen is not entirely bad since small quantities of oxygen prevent warping of the wafers sliced from the crystal when the wafers are heated in the production of integrated circuits. The amount and uniformity of each concentration in the crystal depends on the motion of the melt during crystal growth. The melt motion is driven by the buoyancy and free-surface thermocapillarity associated with the radial temperature gradient and by the rotations of the crucible and crystal.

The crucible is rotated in order to minimize the effects of any slight azimuthal variations in the heating. The thermal convection can involve an undesirable, large-scale periodic motion, but this motion can be suppressed by rotating both the crucible and crystal with certain different angular velocities. The rotation and

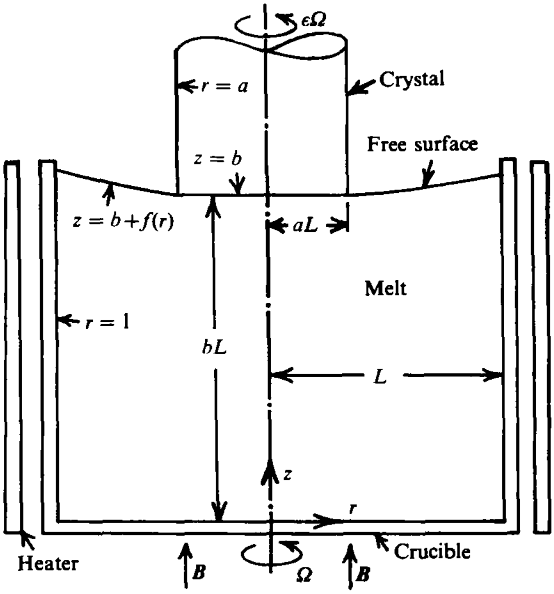

FIGURE 1. Czochralski crystal growth with a uniform, axial magnetic field $\boldsymbol{B}$. The cylindrical coordinates r and z are normalized with the inside radius of the crucible.

shearing stabilize the flow, and the centrifugal pumping in the crystal-face boundary layer can overwhelm the radially inward flow due to thermal convection. The meridional motion (in vertical planes through the centreline) then consists of two circulation cells: one small cell under the crystal face and one large cell with flow out along the crucible bottom, up the vertical crucible wall, in along the free surface and deflected down at the crystal's edge by the smaller cell (Langlois 1981). This two-cell circulation prevents direct flow from the crucible to the crystal and produces a more uniform radial oxygen distribution in the crystal because of its radially outward mass transport on the crystal face.

Even after the large-scale periodic component of the thermal convection is suppressed, there is still small-scale, statistical periodicity because the flow is turbulent. One benefit of the turbulence is that it produces more uniform concentrations in the melt at each instant, which result in more radially uniform concentrations in the crystal. The enhanced mass transport of oxygen due to turbulence can be either a benefit or a penalty: enhanced oxygen transport to the free surface is a benefit, but enhanced transport to the crystal is a penalty. The principal disadvantage of the turbulence is that it produces fluctuations in the heat transfer to the crystal. The crystal growth rate is a function of the local temperature gradient, so that, if this temperature gradient fluctuates, then the growth rate fluctuates. The crystal structure then has very undesirable microscopic non-uniformities.

Since molten silicon has an electrical conductivity which is comparable to that of mercury, the turbulence can be suppressed by applying a magnetic field during crystal growth. The magnetic field also suppresses the steady components of the meridional circulations, thus decreasing the total oxygen transport to both the crystal and the free surface. However, when we suppress turbulence and thermal convection, we lose their benefits as well as their penalties. In particular, we lose the turbulent transport between the streamlines of the motion, which keeps the oxygen and dopant concentrations uniform in the melt. Thus we may gain microscopic structural uniformity at the cost of unacceptable radial variations of oxygen and dopant concentrations in the crystal. In addition, the amount of oxygen in the crystal depends on the relationship between the oxygen transport rates to the crystal and to the free surface. A greater reduction in the transport to the free surface than in that to the crystal produces a larger oxygen concentration in the crystal, particularly in the part grown at the end of the process because it ingests the accumulated reservoir of oxygen in the melt. With magnetic Czochralski, we need a much better understanding of the melt motions, so that we can hopefully find a combination of crucible and crystal rotation rates for each magnetic field strength, which produces crystals with both microscopic and macroscopic uniformity of structure and concentrations.

This paper presents analytical solutions for the melt motions in a Czochralski crucible with a steady, uniform, axial magnetic field, produced by a solenoid placed around the heaters (Hoshikawa 1982 or Kim, Schwuttke & Smetana 1981). Previous treatments involve finite-difference solutions of the Navier–Stokes, heat and Maxwell's equations (Langlois & Walker 1982). There are several advantages to the present analytical solutions. First, analytical techniques permit the discovery and investigation of some physical phenomena which can easily be lost in the complexity of the numerical analysis. For example, we show here that the small electrical currents which flow through the crystal play a key role in determining the melt motion. All previous treatments have erroneously assumed that the crystal is an electrical insulator because its conductivity is only 3 % of that of molten silicon. The analysis reveals that an important electrical current is that in the boundary layer on the crystal face. This boundary layer has a high electrical resistance because it is thin, so its resistance is comparable to that of the crystal. The boundary layer and the crystal are resistors in parallel, and the division of the electrical current between them strongly affects the melt motion.

The melt motion depends on the magnetic field strength, on the angular velocities of the crystal and of the crucible, and on the instantaneous melt depth. As their second benefit, the analytical solutions facilitate the investigation of melt motions for all possible combinations of field strength, angular velocities and melt depth. On the other hand, it is impractical to repeat the numerical analysis for very many points in this rather formidable parameter space. The analysis reveals that the flow pattern sometimes changes radically with quite small changes in the ratio of the angular velocities, so that certain very important, but narrow, ranges of this ratio can be easily missed in a numerical sampling.

The flow with an axial magnetic field is axisymmetric, but the flow with a steady, transverse magnetic field is three-dimensional. The third benefit of the present analytical approach is that it can be applied with comparable effort to the three-dimensional flows with transverse fields, and the results of this three-dimensional analysis will be presented in a future paper. On the other hand, the size of the data arrays needed for reasonable resolution for a three-dimensional flow make the numerical treatment of flows with transverse magnetic fields impractical.

In a typical Czochralski furnace, the crystal grows at a rate of 2.3×10^{-5} m/s, while the melt depth decreases at a rate of 4.2×10^{-6} m/s. These velocities are so small that we can treat the melt motion as a steady flow with constant melt depth and with zero axial velocity on the crystal face. However, we must investigate the flows for different melt depths in order to see how the melt motion evolves during the growth of a crystal.

We assume that the magnetic field strength B is sufficiently large that viscous effects are confined to boundary and free shear (interior) layers, and that the inertial forces associated with the meridional motion are everywhere negligible compared to the electromagnetic (EM) body force. The key to this inertialess assumption is that the meridional velocity decreases as B^{-2}, while the EM body force increases as B^2, as B increases, so that the interaction parameter, which must be large, increases as B^4. We conclude that the present inertialess analysis does not apply for a typical crystal grower with $B = 0.05$ tesla (500 gauss), provides a rough, but qualitatively correct, picture for $B = 0.1$ T, and improves very rapidly as B increases. This conclusion is tentative because there are no published experimental results to confirm it, and it is based on a rough comparison with erroneous numerical results.

The azimuthal motion is independent of the meridional one, and solutions for the azimuthal velocity and associated variables are presented in §3. The meridional motions driven by the centrifugal force associated with the azimuthal velocity and by buoyancy can be treated separately, and solutions for the motion due to the centrifugal force are presented in §§4 and 5. For the buoyancy, the momentum and Maxwell's equations give explicit expressions for the velocity, pressure and free-surface deflection in terms of the unknown temperature. Introducing the sum of the buoyancy and centrifugal-force velocities into the heat equation gives a nonlinear equation involving only one unknown, temperature. This equation can be solved analytically for the boundary and free shear layers, but numerical analysis is required for the inviscid core regions, where thermal convection and conduction are comparable. The necessity of numerical analysis again limits our ability to explore all possible combinations of the controlling parameters. Here, we investigate the isothermal motion and identify parameter combinations which give promising flow patterns. In a future paper we will present numerical solutions of the heat equation for these particular parameter combinations.

2. Problem formulation

Our first assumption is that the Boussinesq approximation holds, i.e. density variations are ignored except in the gravitational body force, and here the density is a linear function of temperature. All other physical properties are assumed to be constant. Our second assumption is that the magnetic Reynolds number

$$R_{\mathrm{m}} = \mu\sigma\Omega L^2 \ll 1,$$

so that we can neglect the magnetic field produced by the electrical currents in the melt and in the crystal. Here, μ and σ are the magnetic permeability and electrical conductivity of the melt, while Ω and L are the angular velocity and inside radius of the crucible (see figure 1). For silicon in a standard 8-inch crucible ($L = 9.44$ cm), rotating at $\Omega = 1.571$ rad/s (15 rev/min), $R_{\mathrm{m}} = 0.0176$. This case is used for all parameter values. With these assumptions, the governing equations for steady melt flows are

$$\rho(\boldsymbol{v}\cdot\nabla)\,\boldsymbol{v} = -\nabla p - \rho g\,[1-\alpha(T-T_0)]\,\hat{\boldsymbol{z}} + \boldsymbol{j}\times\boldsymbol{B} + \rho\nu\nabla^2\boldsymbol{v}, \tag{1a}$$

$$\nabla\cdot\boldsymbol{v} = 0, \quad \boldsymbol{j} = \sigma(-\nabla\phi + \boldsymbol{v}\times\boldsymbol{B}), \tag{1b, c}$$

$$\nabla\cdot\boldsymbol{j} = 0, \quad \boldsymbol{v}\cdot\nabla T = \kappa\nabla^2 T \tag{1d, e}$$

(see Langlois & Walker 1982). Here, the variables $\boldsymbol{v}$, p, T, $\boldsymbol{j}$ and ϕ are the velocity, pressure, temperature, electric-current density and electric potential function (voltage), while the physical constants ρ, α, ν and κ are the density at the reference temperature T_0, the thermal expansion coefficient, the kinematic viscosity and the thermal diffusivity. In addition, $\boldsymbol{B} = B\hat{\boldsymbol{z}}$ is the applied, axial, uniform magnetic field, $\hat{\boldsymbol{z}}$ is a unit vector and g is the gravitational acceleration.

For axisymmetric motion, the variables are independent of θ, where (r, θ, z) are cylindrical coordinates with r and z normalized by L. For the azimuthal velocity v_θ, the characteristic velocity is ΩL. There are two body forces driving the meridional circulation in $\theta =$ constant planes, namely buoyancy and the centrifugal force associated with v_θ, while the electromagnetic (EM) body force, $\boldsymbol{j} \times \boldsymbol{B}$, opposes this motion. Force balances give two characteristic meridional velocities,

$$v_c = \frac{\rho \Omega^2 L}{\sigma B^2}, \quad v_b = \frac{\rho g \alpha (\Delta T)}{\sigma B^2},$$

for the centrifugal and buoyancy forces, respectively, where ΔT is a characteristic temperature difference. The ratio

$$v_{bc} = \frac{v_b}{v_c} = \frac{g\alpha(\Delta T)}{\Omega^2 L} = 0.0522,$$

with $\Delta T = 88$ °C. Therefore, v_c is the appropriate characteristic meridional velocity.

The dimensionless variables (denoted here by asterisks) are defined by:

$$\begin{aligned}
&v_r = v_c v_r^*, \quad v_\theta = \Omega L v_\theta^*, \quad v_z = v_c v_z^*,\\
&j_r = \sigma \Omega L B j_r^*, \quad j_\theta = \sigma v_c B j_\theta^*,\\
&j_z = \sigma \Omega L B j_z^*, \quad \phi = \Omega L^2 B \phi^*,\\
&T = T_0 + (\Delta T) T^*, \quad p = \rho g L (b - z) + \rho \Omega^2 L^2 p^*,
\end{aligned}$$

where bL is the instantaneous melt depth under the crystal. Henceforth, all variables are dimensionless, so we drop the asterisks. For these dimensionless variables, (1) becomes

$$N^{-1} D v_r - \frac{v_\theta^2}{r} = -\frac{\partial p}{\partial r} + j_\theta + M^{-2}\left(\nabla^2 v_r - \frac{v_r}{r^2}\right), \tag{2a}$$

$$N^{-1}\left(D v_\theta + \frac{v_r v_\theta}{r}\right) = -j_r + M^{-2}\left(\nabla^2 v_\theta - \frac{v_\theta}{r^2}\right), \tag{2b}$$

$$N^{-1} D v_z = -\frac{\partial p}{\partial z} + v_{bc} T + M^{-2} \nabla^2 v_z, \tag{2c}$$

$$\frac{\partial v_r}{\partial r} + \frac{v_r}{r} + \frac{\partial v_z}{\partial z} = 0, \quad \frac{\partial j_r}{\partial r} + \frac{j_r}{r} + \frac{\partial j_z}{\partial z} = 0, \tag{2d, e}$$

$$j_r = -\frac{\partial \phi}{\partial r} + v_\theta, \quad j_\theta = -v_r, \tag{2f, g}$$

$$j_z = -\frac{\partial \phi}{\partial z}, \quad Pe\, DT = \nabla^2 T, \tag{2h, i}$$

where

$$D = v_r \frac{\partial}{\partial r} + v_z \frac{\partial}{\partial z}, \quad \nabla^2 = \frac{\partial^2}{\partial r^2} + \frac{1}{r}\frac{\partial}{\partial r} + \frac{\partial^2}{\partial z^2}.$$

The parameters are the interaction parameter, Hartmann number and Péclet number, which are defined by

$$N = \frac{\sigma B^2 L}{\rho v_c} = \frac{\sigma^2 B^4}{\rho^2 \Omega^2}, \quad M = BL\left(\frac{\sigma}{\rho \nu}\right)^{\frac{1}{2}}, \quad Pe = \frac{v_c L}{\kappa} = \frac{\rho \Omega^2 L^2}{\sigma \kappa B^2},$$

B (T)	N	M	Pe
0.05	0.466	178.5	1640
0.10	7.463	357.1	410.0
0.20	119.4	714.1	102.5
0.30	604.5	1071	45.55
0.50	4665	1785	16.40

TABLE 1. Values of the interaction parameter N, the Hartmann number M and the Péclet number Pe for molten silicon in a crucible with an inside radius of 9.44 cm, rotating at 1.571 rad/s, for various magnetic field strengths B

respectively. Values of these parameters for $B = 0.05$–0.5 tesla (500–5000 gauss) are given in table 1.

The thermal boundary conditions will be discussed in a future paper. The quartz crucible is an electrical insulator, so that the boundary conditions at the crucible bottom and vertical wall are:

$$v_r = v_z = j_z = 0, \quad v_\theta = r, \quad \text{at } z = 0, \qquad (3a\text{–}d)$$

$$v_r = v_z = j_r = 0, \quad v_\theta = 1, \quad \text{at } r = 1. \qquad (3e\text{–}h)$$

We neglect the surface tension of the free surface. The importance of thermocapillarity will be discussed in a future paper. The atmosphere above the free surface is an electrical insulator, so that the boundary conditions at the free surface are:

$$v_n = j_n = \frac{\partial v_\theta}{\partial n} = \frac{\partial v_t}{\partial n} = 0, \qquad (4a\text{–}d)$$

$$f = F(p - M^{-2}\,\partial v_n/\partial n), \quad \text{at } z = b + f(r), \qquad (4e)$$

for $a \leqslant r \leqslant 1$. Here, n and t are coordinates normal and tangent to the free surface in meridional planes, aL is the crystal radius, and

$$F = \frac{\Omega^2 L}{g} = 0.0238$$

is the Froude number for the azimuthal motion. Since p is the deviation of the pressure from a hydrostatic pressure with constant density and with $p = 0$ at $z = b$, the boundary condition (4e) for large M simply states that, if a body force produces a deviation pressure p, then the free surface is deflected appropriately in order to keep the total pressure at the free surface equal to zero. The velocity boundary conditions at the crystal face are:

$$v_r = v_z = 0, \quad v_\theta = \epsilon r, \quad \text{at } z = b, \qquad (5a\text{–}c)$$

for $0 \leqslant r \leqslant a$, where $\epsilon\Omega$ is the angular velocity of the crystal's rotation, and $\epsilon < 0$ if the crystal and crucible are rotated in opposite directions (counter-rotation).

The electrical conductivity of the crystal, $\delta\sigma$, is much less than that of the melt. Near the crystallization temperature, the ratio δ of the silicon crystal's conductivity to that of molten silicon is 0.0316. Since δ is small, previous studies have treated the crystal as an electrical insulator (Langlois & Walker 1982). However, it turns out that the crystal acts as a resistor in parallel to the boundary layer in the melt on the crystal face, and the small electrical currents in the crystal strongly influence the melt motion. In the crystal, the governing dimensional equations are the equations (1c, d)

with σ replaced by $\delta\sigma$ and with the crystal velocity given by $\epsilon\Omega L r\hat{\theta}$, where $\hat{\theta}$ is a unit vector. Using the same normalization, the equations governing the dimensionless electric-current density $\boldsymbol{j}_s$ and electric potential function ϕ_s in the crystal are:

$$j_{rs} = \delta\left(-\frac{\partial\phi_s}{\partial r}+\epsilon r\right), \quad j_{zs} = -\delta\frac{\partial\phi_s}{\partial z}, \tag{6a, b}$$

$$\frac{\partial j_{rs}}{\partial r}+\frac{j_{rs}}{r}+\frac{\partial j_{zs}}{\partial z} = 0. \tag{6c}$$

The boundary conditions on the crystal variables are:

$$j_{rs} = 0, \quad \text{at } r = a, \quad \text{for } z \geqslant b, \tag{7a}$$

$$\boldsymbol{j}_s \rightarrow 0, \quad \text{as } z \rightarrow \infty, \tag{7b}$$

$$j_{zs} = j_z, \quad \phi_s = \phi, \quad \text{at } z = b. \tag{7c, d}$$

The condition (7*b*) assumes an infinitely long crystal, which is not realistic. However, it turns out that 96 % of the crystal's electrical current is confined to the bottom length of the crystal equal to two-thirds of the crystal radius, i.e. in $b \leqslant z \leqslant b+\frac{2}{3}a$. Therefore, once the crystal length is comparable to its radius, the length is effectively infinite for the electrical problem, and the condition (7*b*) is realistic. The conditions (7*c*, *d*) state that the normal current and the voltage are continuous across the crystal–melt interface.

Here, the crucible bottom and the crystal face are assumed to be plane and parallel. An actual crucible has a spherical bottom with a large radius (45.1 cm for a standard 8-inch crucible). In addition, the crystal face is an isotherm for the thermal-conduction problem in the crystal. The crystal receives heat from the melt and loses it by radiation and conduction from the exposed surface, so that isotherms, including the crystal face, are concave upward. Therefore, the crucible bottom and crystal face are not actually parallel. Previous studies of magnetohydrodynamic flows have indicated that the flow between slightly divergent surfaces may be radically different from that between parallel surfaces, and that slopes become significant when they are comparable to M^{-1} (Petrykowski & Walker 1984). The values in table 1 indicate that M^{-1} is quite small, so we have also treated the flow in a crucible with a large-radius spherical bottom and with a slightly concave crystal face. The results are virtually identical with those for the geometry in figure 1, so that the present geometrical simplifications are justified.

Our third assumption about parameter values is that N is sufficiently large that the terms in the equations (2*a*–*c*) which are multiplied by N^{-1} can be neglected everywhere. The values in table 1 indicate that this inertialess approximation is certainly invalid for $B = 0.05$ T, and roughly correct at best for $B = 0.1$ T, but that it improves rapidly as B increases. We note that our first assumption involves a parameter since the Boussinesq approximation is the leading term in an asymptotic expansion for small values of the parameter $\alpha(\Delta T)$, which is 0.00124 here.

Our fourth parametric assumption is that $M \gg 1$, so that M^{-1} is the small parameter for asymptotic expansions for the flow variables in certain subregions of the melt. The subregions (shown in figure 2) are the outer (o) and inner (i) cores with all dimensions $O(1)$, the Hartmann layers (h) with $O(M^{-1})$ thickness, the free shear layer (f) at $r = a$ with $O(M^{-\frac{1}{2}})$ thickness, the vertical wall layer (w) at $r = 1$ with $O(M^{-\frac{1}{2}})$ thickness, and the intersection regions (I) with $O(M^{-1}) \times O(M^{-\frac{1}{2}})$ dimensions in meridional planes. The free shear and vertical wall layers are thicker than the

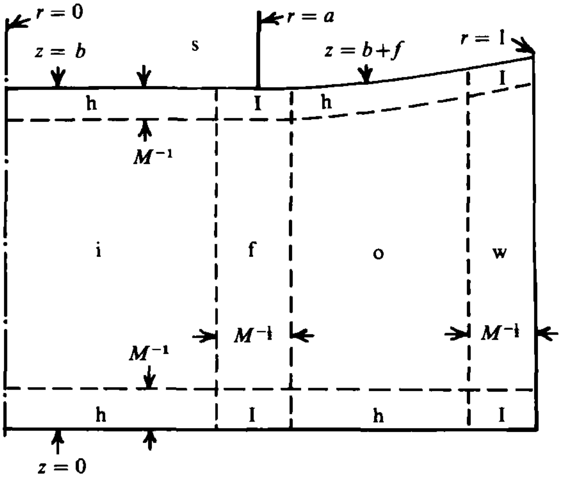

FIGURE 2. Meridional section showing subregions of the melt for $M \gg 1$.

Hartmann layers because the former are parallel to the applied magnetic field (Petrykowski & Walker 1984). The variables in each subregion are written as appropriate asymptotic expansions for large M, and the expansions in adjacent regions are matched. Henceforth, a variable with a subscript, i, o, f, etc. denotes the leading term in the asymptotic expansion for that variable in the inner core, outer core, free shear layer, etc.

The inertialess approximation neglects the meridional convection of the angular momentum in the azimuthal motion, which is represented by the left-hand side of (2*b*). As a result, the boundary-value problem for the azimuthal motion can be solved independently of the meridional problem, and this solution is presented in the next section.

3. Azimuthal motion

The variables v_θ, j_r, j_z and ϕ are governed by the modified equation (2*b*) with the left-hand side replaced by zero, by the equations (2*e*,*f*, *h*, 6), and by the boundary conditions (3*c*, *d*, *g*, *h*, 4*b*, *c*, 5*c*,7). In the outer core, adjacent Hartmann layers, vertical wall layer and adjacent intersection regions, the solution

$$v_\theta = r, \quad \phi = C_1 + \tfrac{1}{2}r^2, \quad j_r = j_z = 0, \qquad (8a\text{–}c)$$

satisfies the equations (2*b*, *e*, *f*, *h*) and the conditions (3*c*, *d*, *g*, *h*, 4*b*, *c*) identically, i.e. to all orders in M. Here, C_1 is a constant voltage. The only possible perturbation to this rigid-body rotation with the crucible would arise in matching the free-shear-layer solution. However, we have found the first three terms in the asymptotic solution for the free shear layer, and all three match this rigid-body rotation for $r > a$ without perturbing it.

In actual crystal growth with an axial magnetic field, the principal perturbation of this outer rigid-body rotation arises because of thermal convection in meridional planes. As fluid near the bottom moves outward, its v_θ decreases to conserve angular momentum. Similarly, as fluid near the free surface moves inward, its v_θ increases. Since the radial voltage gradient, $\partial\phi/\partial r$, is proportional to v_θ, the voltage difference between $r = a$ and $r = 1$ is greater at the free surface than at the bottom, and this vertical variation of the voltage difference drives a circulation of electric current in meridional planes. The EM body force due to this current slows the fluid near the free surface and accelerates the fluid near the bottom, thus restoring the rigid-body motion. As the magnetic-field strength increases, the EM body force is much greater than the angular momentum transport, i.e. a slight deviation from rigid-body motion produces a small current, which in turn produces a sufficiently large EM body force to restore rigid-body motion. Langlois & Lee (1983) include inertial effects, treat the crystal as an electrical insulator and present numerical results for the meridional circulation of electric current in their figures 2 and 4. For comparison with the inertialess solution (8), we are interested in their current lines beyond the crystal edge, i.e. for $r > a$. In their figure 2, the numbers of current lines here are 6 for $B = 0.05$ T, 3 for $B = 0.1$ T and 1 for $B = 0.2$ T. In their figure 4 (with α multiplied by 10 to investigate high buoyancy), the numbers of current lines here are approximately 30 for $B = 0.05$ T, 10 for $B = 0.1$ T and 1 for $B = 0.2$ T. Their numerical results with inertial effects confirm the earlier statement about the validity of the inertialess approximation, namely that it is invalid for $B = 0.05$ T, rough at best for $B = 0.1$ T and probably reasonably accurate for $B = 0.2$ T.

In the inner core, the variables are written as asymptotic expansions, such as $\phi = \phi_i + M^{-1}\phi_i' + O(M^{-2})$, where the prime distinguishes the $O(M^{-1})$ perturbations from the $O(1)$ solutions. The equations (2*b, e, f, h*) then give

$$j_{ri} = 0, \quad \phi_i = \Phi_i - z j_{zi}, \quad v_{\theta i} = \frac{\partial \phi_i}{\partial r}, \tag{9}$$

where Φ_i and j_{zi} are functions of r only. The $O(M^{-1})$ solutions are given by the same expressions with primes added to all variables.

The jump in the normal current across a Hartmann layer is $O(M^{-1})$, so that the boundary condition (3*c*) indicates that the $O(1)$ inner-core solutions are

$$j_{ri} = j_{zi} = 0, \quad \phi_i = \Phi_i, \quad v_{\theta i} = \frac{\mathrm{d}\Phi_i}{\mathrm{d}r}. \tag{10a–d}$$

For the Hartmann layer at the bottom for $r < a$, the axial coordinate is stretched by substituting $Z = Mz$, while j_{rh}, ϕ_h and $v_{\theta h}$ denote $O(1)$ quantities, but j_{zh} denotes an $O(M^{-1})$ quantity. After the coordinate stretching, the equation (2*h*) gives $\phi_h = \Phi_i$, while the equations (2*b,f*) govern j_{rh} and $v_{\theta h}$. The solutions which satisfy the boundary condition (3*d*) and which match the $O(1)$ inner-core solutions (10) are

$$v_{\theta h} = v_{\theta i} + (r - v_{\theta i}) \exp(-Z), \tag{11a}$$

$$j_{rh} = (r - v_{\theta i}) \exp(-Z). \tag{11b}$$

The result (11*b*) is introduced into (2*e*) governing j_{zh}, and the solution which satisfies the boundary condition (3*c*) is

$$j_{zh} = r^{-1}[\exp(-Z) - 1] \frac{\mathrm{d}}{\mathrm{d}r}(r^2 - r v_{\theta i}). \tag{12}$$

Matching the $O(M^{-1})$ axial currents in the bottom Hartmann layer and inner core determines j_{zi}', and the solutions (9), with primes added, are

$$j_{zi}' = -r^{-1} \frac{\mathrm{d}}{\mathrm{d}r}(r^2 - r v_{\theta i}), \quad \phi_i' = \Phi_i' - z j_{zi}', \tag{13a,b}$$

$$v_{\theta i}' = \frac{\mathrm{d}\Phi_i'}{\mathrm{d}r} - z \frac{\mathrm{d}j_{zi}'}{\mathrm{d}r}, \quad j_{ri}' = 0. \tag{13c,d}$$

The $O(1)$ inner-core $v_{\theta\mathrm{i}}$ (10d) is independent of z, so all the fluid on a cylinder r = constant has the same azimuthal velocity, although there may be shear between cylinders of different radii. The bottom Hartmann-layer structure, which accommodates a difference between $v_{\theta\mathrm{i}}$ and $v_\theta = r$ on the crucible bottom, requires a radial current to produce the EM body force to balance the viscous shear force. This radial current must come from the inner core, and this requires an $O(M^{-1})$ vertical inner-core current from the top Hartmann layer to the bottom one. An $O(M^{-1})$ linear voltage drop from the crystal to the crucible is required to drive this vertical inner-core current. The azimuthal momentum equation (2b) indicates that there is no force to balance the EM body force due to j_r in the core, so $j_r = 0$ here, neglecting $O(M^{-2})$ terms. The radial component of Ohm's law (2f) then implies that the induced voltage $(\boldsymbol{v}\times\boldsymbol{B})_r = v_\theta$ must cancel the radial voltage gradient, so $v'_{\theta\mathrm{i}} = \partial\phi'_\mathrm{i}/\partial r$. If $v_{\theta\mathrm{i}}$ is a rigid body rotation, then $j'_{z\mathrm{i}}$ is uniform, the axial voltage drop is independent of r, and $v'_{\theta\mathrm{i}}$ is independent of z. However, if $v_{\theta\mathrm{i}}$ deviates from some rigid-body rotation, then the $j'_{z\mathrm{i}}$ needed by the bottom Hartmann layer varies with r, so the axial voltage drop driving this current must also vary with r. Since the induced voltage due to $v'_{\theta\mathrm{i}}$ must balance the radial voltage gradient at each horizontal level, $v'_{\theta\mathrm{i}}$ has a linear variation with z, which is represented by the last term in (13c). In the next section, we treat the meridional motion driven by the centrifugal force associated with v_θ, and the axial variation of $v'_{\theta\mathrm{i}}$ turns out to be important. Here we see that this variation is due to the electrical current requirements of the bottom Hartmann layer.

For the Hartmann layer on the crystal face, the axial coordinate is stretched by substituting $Z' = M(z-b)$. The $O(1)$ top-Hartmann-layer variables which satisfy the stretched versions of the equations (2b,f,h), as well as the boundary condition (5c), and which match the $O(1)$ inner-core solutions (10) are

$$\phi_\mathrm{h} = \Phi_\mathrm{i}, \quad j_{r\mathrm{h}} = (\epsilon r - v_{\theta\mathrm{i}}) \exp(Z'), \tag{14a,b}$$

$$v_{\theta\mathrm{h}} = v_{\theta\mathrm{i}} + (\epsilon r - v_{\theta\mathrm{i}}) \exp(Z'). \tag{14c}$$

The result (14b) is substituted into the stretched equation (2e), which governs the $O(M^{-1})$ top-Hartmann-layer current $j_{z\mathrm{h}}$. The solution which matches the inner-core solution (13a) is

$$j_{z\mathrm{h}} = -r^{-1}\frac{\mathrm{d}}{\mathrm{d}r}(r^2 - r v_{\theta\mathrm{i}}) - r^{-1}\exp(Z')\frac{\mathrm{d}}{\mathrm{d}r}(\epsilon r^2 - r v_{\theta\mathrm{i}}). \tag{15}$$

The inner-core solutions (10, 13) and the Hartmann-layer solutions (11, 12, 14, 15) are expressed in terms of two unknown functions of r, namely Φ_i and Φ'_i, which are determined by solving for the electrical variables in the crystal.

The equations (6a,b) are introduced into (6c) and the boundary conditions (7a,b) to obtain the equation

$$\nabla^2\phi_\mathrm{s} = 2\epsilon, \tag{16}$$

and the boundary conditions

$$\partial\phi_\mathrm{s}/\partial r = \epsilon a, \quad \text{at } r = a, \tag{17a}$$

$$\phi_\mathrm{s} \rightarrow \tfrac{1}{2}\epsilon r^2, \quad \text{as } z \rightarrow \infty, \tag{17b}$$

where the voltage at $r = 0$ is set equal to zero with no loss of generality. The separation of variables solution for the problem (16, 17) is

$$\phi_\mathrm{s} = \tfrac{1}{2}\epsilon r^2 + \sum_{j=1}^{\infty} c_j J_0(X_j R) \exp\left[-\frac{X_j(z-b)}{a}\right], \tag{18}$$

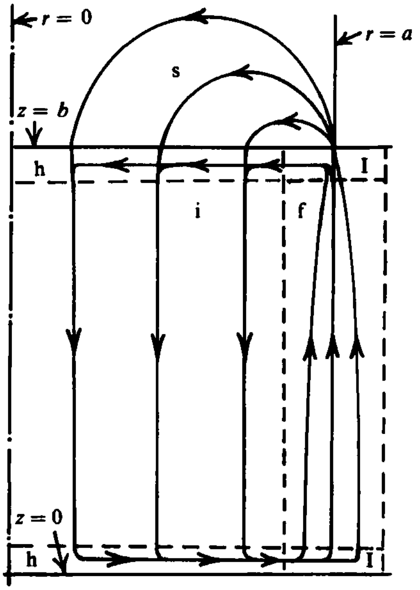

FIGURE 3. Sketch of the meridional current lines for the $O(M^{-1})$ electric current.

where X_j are the zeros of J_1, J_0 and J_1 are the Bessel functions of the first kind of zeroth and first order, and $R = r/a$, i.e. the radial coordinate normalized by the crystal radius.

The problem (16, 17) does not involve M, so the solution (18) applies to all orders, i.e. the term $\frac{1}{2}\epsilon r^2$ goes with the $O(1)\,\phi_s$, and each order of ϕ_s has its own set of coefficients c_j. The asymptotic expansion, $\phi_s = \phi_s + M^{-1}\phi_s' + O(M^{-2})$, is required because these solutions must match the top-Hartmann-layer solutions through the conditions (7*c*, *d*). The condition (7*d*) and the solution (14*a*) give $\Phi_{\mathrm{i}} = \phi_s(r, b)$, so the $O(1)$ voltage throughout the inner core and adjacent Hartmann layers is given by the $O(1)$ crystal voltage at the crystal face. The equations (6*a*, *b*) indicate that ϕ_s drives an $O(\delta)$ electric current, which is small because the relative electrical conductivity of the crystal, δ, is small ($\delta = 0.0316$ for silicon). At the crystal face, the axial component of the small crystal current must equal the small axial current in the top Hartmann layer, so that the boundary condition (7*c*), together with the equations (6*d*, 10*d*, 14*a*, 15), becomes

$$\delta\frac{\partial\phi_s}{\partial z} = M^{-1}r^{-1}\frac{\partial}{\partial r}\left[(1+\epsilon)\,r^2 - 2r\frac{\partial\phi_s}{\partial r}\right] \quad \text{at } z = b. \qquad (19)$$

This condition determines the coefficients for the $O(1)$ crystal voltage (18):

$$c_j = -\frac{2a^2(1-\epsilon)}{X_j(\gamma+2X_j)\,J_2(X_j)},$$

where $\gamma = a\delta M$.

The solution, $(\phi_s - \frac{1}{2}\epsilon r^2)/a^2(1-\epsilon)$, is a function of R and $(z-b)/a$, i.e. the axial distance from the crystal face normalized by the crystal radius, and depends on a single parameter γ. The current lines for the $O(M^{-1})$ electric current in meridional planes are sketched in figure 3. We previously found an electric current flowing down through the inner core and outward through the bottom Hartmann layer. This

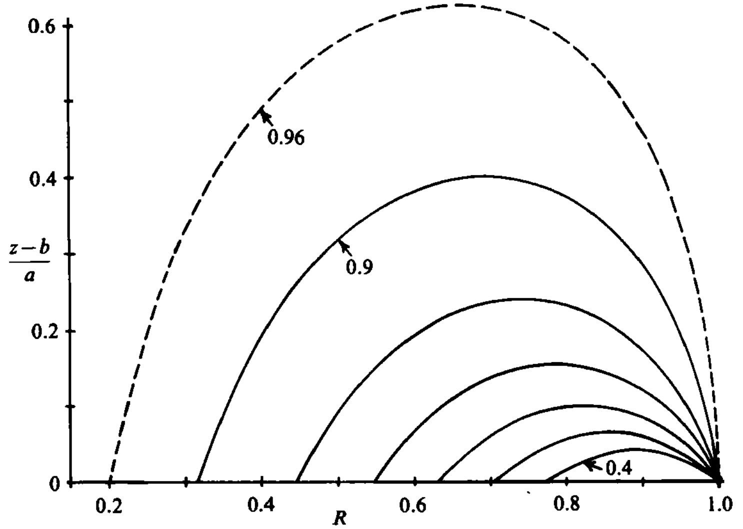

FIGURE 4. Electric current lines in the crystal for $\gamma \gg 1$. The current streamfunction is normalized to have a value of one for the total crystal current. Values for the solid lines vary from 0.4 to 0.9 in steps of 0.1.

current flows up through the free shear layer and splits at the top intersection region with part flowing radially inward through the crystal and part through the top Hartmann layer. Both the crystal and top Hartmann layer have large electrical resistances, the former because its relative conductivity δ is small, and the latter because its $O(M_s^{-1})$ thickness is small. Here $M_s = aM$ is the Hartmann number based on the crystal radius. The ratio of these two large, parallel resistances is reflected in $\gamma = \delta/M_s^{-1} = a\delta M$. If $\gamma \ll 1$, the crystal is an electrical insulator, and all the $O(M^{-1})$ current flows through the top Hartmann layer. In this case, the radial currents in the top and bottom Hartmann layers are equal and opposite, and the jumps in v_θ for these two layers are equal. Therefore, $v_{\theta i} = \frac{1}{2}(1+\epsilon)r$, i.e. the inner core rotates as a rigid body with the average of the crystal and crucible angular velocities. At the other extreme, $\gamma \gg 1$, the crystal is a much better conductor than the top Hartmann layer, and all the current flows through the crystal with only an $O(\gamma^{-1})$ deviation of ϕ_s from $\frac{1}{2}\epsilon r^2$. Since there is no current in the top Hartmann layer, there is no jump in v_θ across the layer, and $v_{\theta i} = \epsilon r$, i.e. the inner core rotates as a rigid body with the crystal. The jump in v_θ across the bottom Hartmann layer for $\gamma \gg 1$, is twice that for $\gamma \ll 1$, so there is twice as much $O(M^{-1})$ electric current circulating. The current lines in the crystal for $\gamma \gg 1$ are presented in figure 4. The crystal sees a source of electric current at its bottom edge, $r = a$, $z = b$, which represents the current entering from the top intersection region. Most (96 %) of the crystal current circulates below the dashed line in figure 4. This dashed line reaches up to $z = b + 0.625a$, which illustrates the earlier statement that the current is mostly confined to the bottom length of the crystal equal to less than two-thirds of a crystal radius.

As γ decreases from infinity to zero, the total current decreases by a factor of two, the fraction of this current flowing in the crystal decreases from one to zero, and the inner core azimuthal motion shifts from a rigid-body rotation with the crystal angular velocity to a rigid-body rotation with the average angular velocity. However, at finite

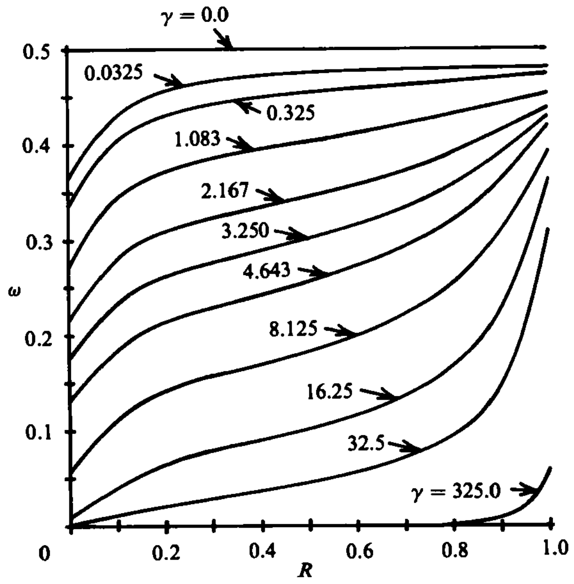

FIGURE 5. Relative angular velocity function for the inner-core azimuthal velocity.

values of γ, there is a radial variation of the electric current division between the crystal and the top Hartmann layer. Figure 4 shows that the current entering the crystal directly from the intersection region sees a small normal area near the crystal edge and therefore sees a large local electrical resistance. Once past this bottleneck, the current spreads over a larger normal area with a correspondingly smaller resistance. Therefore, the effective resistance of the crystal is large at the edge and small elsewhere. On the other hand, the top Hartmann layer has the same $O(M_s^{-1})$ normal area at every radius. For a finite value of γ, the electric current leaving the intersection region sees the large resistance of the crystal edge, so virtually all the current enters the Hartmann layer at $r = a$. As the current flows radially inward, the effective resistance of the adjacent crystal decreases, so the current splits and a significant fraction of it flows up into the crystal for $r < a$. Thus, near $r = a$, the fraction of the total current in the top Hartmann layer is nearly 1, and $v_{\theta i}$ here tends to the average angular velocity times r, but, for $r < a$, this fraction is less than 1, and $v_{\theta i}$ tends more towards motion with the crystal. The inner-core azimuthal motion deviates from rigid-body rotation for finite γ, even though it is two different rigid-body rotations for $\gamma \gg 1$ and $\gamma \ll 1$.

The $O(1)$ inner-core azimuthal velocity can be expressed in terms of a relative angular velocity ω:

$$v_{\theta i} = \epsilon r + r(1-\epsilon)\,\omega, \tag{20}$$

where ω is a function of R and depends only on the parameter γ. The values $\omega = 0$, 1 and 0.5 correspond to rotations with the crystal, with the crucible, and with the average angular velocity, respectively. Graphs of ω for various values of γ are presented in figure 5. The effect of the high electrical resistance of the crystal edge region is particularly evident in the graphs for $\gamma = 8.125$ to 32.5. The angular velocity of the central column of fluid under the centre of the crystal deviates from the crystal's angular velocity by less than 20 % of the crystal–crucible angular-velocity difference, indicating that most of the current at these small radii is in the crystal.

For these values of γ, there is large shearing beyond $R = 0.8$ as the fluid near the free shear layer tends towards the average angular velocity ($\omega = 0.5$), indicating that most of the current near $R = 1$ is in the top Hartmann layer. The effective resistance of the crystal edge region is so great that the motion for $R > 0.8$ deviates significantly from that of the crystal, even for $\gamma = 325$. In the parameter $\gamma = \delta B(aL)(\sigma/\rho\nu)^{\frac{1}{2}}$, everything is a physical constant except the magnetic field strength B and the crystal radius (aL). For an 8 cm diameter silicon crystal, $\gamma = 4.643$, 8.125 and 16.25 correspond to $B = 0.10$ T, 0.17 T and 0.34 T, respectively, which fall in the range of field strengths generally being considered for magnetic Czochralski (Lee, Langlois & Kim 1984). Therefore magnetic Czochralski flows involve large radial shear in the azimuthal motion under the crystal.

The solutions for the $O(M^{-2})$ axial currents in the inner core and adjacent Hartmann layers would be required in order to determine Φ_{i}' by solving for ϕ_{s}'. However, in the $O(M^{-1})$ inner-core solution (13c), the second term representing the axial variation of $v_{\theta\mathrm{i}}'$ is important and is now completely determined, but the first term involving Φ_{i}' merely adds an $O(M^{-1})$ radial pressure gradient. Therefore, the solutions for Φ_{i}' and the associated variables are not presented here.

For the free shear layer, the radial coordinate is stretched by substituting $\zeta = M^{\frac{1}{2}}(r-a)$. The variables are replaced by the asymptotic expansions

$$v_\theta = v_{\theta\mathrm{f}} + M^{-\frac{1}{2}}v_{\theta\mathrm{f}}' + O(M^{-1}),$$

$$\phi = \Phi_{\mathrm{i}}(a) + M^{-\frac{1}{2}}\phi_{\mathrm{f}} + M^{-1}\phi_{\mathrm{f}}' + O(M^{-\frac{3}{2}}),$$

$$j_r = M^{-1}j_{r\mathrm{f}} + M^{-\frac{3}{2}}j_{r\mathrm{f}}' + O(M^{-2}),$$

$$j_z = M^{-\frac{1}{2}}j_{z\mathrm{f}} + M^{-1}j_{z\mathrm{f}}' + O(M^{-\frac{3}{2}}).$$

The equations (2b, e, f, h) become

$$j_{r\mathrm{f}} = \frac{\partial^2 v_{\theta\mathrm{f}}}{\partial\zeta^2} + h_1, \quad \frac{\partial j_{r\mathrm{f}}}{\partial\zeta} + \frac{\partial j_{z\mathrm{f}}}{\partial z} = h_2, \quad \frac{\partial v_{\theta\mathrm{f}}}{\partial z} + \frac{\partial j_{z\mathrm{f}}}{\partial\zeta} = 0, \tag{21a,b,c}$$

and the same equations with a prime added to each term. Here, the equations (2f, h) have been combined to eliminate ϕ and to obtain the equation (21c), while $h_1 = h_2 = 0$,

$$h_1' = a^{-1}\frac{\partial v_{\theta\mathrm{f}}}{\partial\zeta}, \quad h_2' = -a^{-1}j_{r\mathrm{f}}.$$

The intersection regions on the bottom (at $z = 0$, for all ζ) and on the crystal face (at $z = b$, for $\zeta < 0$) have exponential structures to accommodate jumps in v_θ. The solutions for v_θ and j_r in these intersection regions are the same as the solutions (11, 14b, c) with $v_{\theta\mathrm{i}}$ replaced by $v_{\theta\mathrm{f}}$ or $v_{\theta\mathrm{f}}'$ (evaluated at $z = 0, b$) and with r replaced by a or ζ, for the $O(1)$ or $O(M^{-\frac{1}{2}})$ solutions, respectively. To obtain the boundary conditions on $j_{z\mathrm{f}}$ and $j_{z\mathrm{f}}'$ at $z = 0, b$, we introduce the $O(M)$ axial stretching, the $O(M^{\frac{1}{2}})$ radial stretching and the solutions for the radial electric currents in the intersection regions into (2e). We integrate this equation from 0 to arbitrary Z or Z' to obtain the solutions for the $O(M^{-\frac{1}{2}})$ and $O(M^{-1})$ axial currents in the intersection regions. Matching the free-shear-layer solutions gives

$$j_{z\mathrm{f}} = \pm\frac{\partial v_{\theta\mathrm{f}}}{\partial\zeta} + h_3, \quad \text{at } z = 0, b, \tag{22}$$

and the same conditions with a prime added to each term. Here, $h_3 = 0$, the plus applies at $z = 0$, for all ζ, where $h'_3 = a^{-1}v_{\theta \mathrm{f}}(\zeta, 0) - 2$, and the minus applies at $z = b$, for $\zeta < 0$, where

$$h'_3 = -M\delta \frac{\partial \phi_\mathrm{s}}{\partial z}(a, b) - a^{-1}v_{\theta \mathrm{f}}(\zeta, b) + 2\epsilon.$$

The first term in h'_3 at $z = b$ can be expressed in terms of $v_{\theta \mathrm{i}}$ and $\mathrm{d}v_{\theta \mathrm{i}}/\mathrm{d}r$, at $r = a$, using the boundary condition (19) and the result $v_{\theta \mathrm{i}} = \partial \phi_\mathrm{s}/\partial r(r, b)$.

For an intersection region adjacent to a solid surface, the $O(1)$ and $O(M^{-\frac{1}{2}})$ tangential velocities vary exponentially, and these variations lead to $O(M^{-\frac{1}{2}})$ and $O(M^{-1})$ jumps in the normal current and normal velocity across the region, as reflected in the conditions (22). For an intersection region adjacent to a free surface which is nearly perpendicular to the free shear or wall layer, Hays & Walker (1984) show that the $O(1)$ and $O(M^{-\frac{1}{2}})$ tangential velocities are independent of the stretched normal coordinate, thus satisfying the boundary conditions (4*c*, *d*) automatically. If the normal derivatives of the $O(1)$ and $O(M^{-\frac{1}{2}})$ tangential velocities in the free shear or wall layer are not zero at the free surface, then the $O(M^{-1})$ and $O(M^{-\frac{3}{2}})$ tangential velocities in the intersection regions vary exponentially and accommodate the jumps in shear stress across the region. These variations imply $O(M^{-\frac{3}{2}})$ and $O(M^{-2})$ jumps in normal current and normal velocity across the region. The component of the unit normal to the free surface, which is normal to the free shear or wall layer, must be no more than $O(M^{-\frac{1}{2}})$ for these statements to apply, and for the present problem this restriction means that the Froude number is at most $O(M^{-\frac{1}{2}})$, which is indeed the case. Therefore, the boundary condition (4*b*) gives

$$j_{z\mathrm{f}} = j'_{z\mathrm{f}} = 0, \quad \text{at } z = b, \quad \text{for } \zeta > 0. \tag{23}$$

If the component of the surface normal perpendicular to the free shear layer is $O(1)$, i.e. if $F = O(1)$, then $j'_{z\mathrm{f}}$ is given in terms of $\partial j_{z\mathrm{f}}/\partial z$, $j_{r\mathrm{f}}$ and $\partial v_{\theta \mathrm{f}}/\partial \zeta$, at $z = b$, but these three functions turn out to be zero here, so the conditions (23) actually apply with no restrictions on the Froude number.

Matching the free-shear-layer variables with the inner- and outer-core solutions (8, 10, 13) gives $C_1 = \Phi_1(a) - \frac{1}{2}a^2$, as well as

$$v_{\theta \mathrm{f}} \rightarrow h_4, \quad j_{r\mathrm{f}} \rightarrow 0, \quad j_{z\mathrm{f}} \rightarrow h_5, \quad \text{as } \zeta \rightarrow -\infty, \tag{24a–c}$$

$$v_{\theta \mathrm{f}} \rightarrow h_6, \quad j_{r\mathrm{f}} \rightarrow 0, \quad j_{z\mathrm{f}} \rightarrow 0, \quad \text{as } \zeta \rightarrow \infty, \tag{24d–f}$$

and the same conditions with a prime added to each term. Here

$$h_4 = v_{\theta \mathrm{i}}(a), \quad h'_4 = \zeta \frac{\mathrm{d}v_{\theta \mathrm{i}}}{\mathrm{d}r}(a),$$

$$h_5 = 0, \qquad h'_5 = \frac{\mathrm{d}v_{\theta \mathrm{i}}}{\mathrm{d}r}(a) + a^{-1}v_{\theta \mathrm{i}}(a) - 2,$$

$$h_6 = a, \qquad h'_6 = \zeta.$$

The solutions of the problems (21–24) are

$$v_{\theta \mathrm{f}} = \tfrac{1}{2}[a + v_{\theta \mathrm{i}}(a)] + \tfrac{1}{2}[a - v_{\theta \mathrm{i}}(a)]\,E, \tag{25a}$$

$$v'_{\theta \mathrm{f}} = \tfrac{1}{2}[1 - a^{-1}v_{\theta \mathrm{i}}(a)]\,e + \tfrac{1}{2}\zeta\left[1 + \frac{\mathrm{d}v_{\theta \mathrm{i}}}{\mathrm{d}r}(a)\right] + \frac{1}{2}\left[1 - \frac{\mathrm{d}v_{\theta \mathrm{i}}}{\mathrm{d}r}(a)\right](\zeta E + 2e), \tag{25b}$$

where
$$E = \operatorname{erf}[\tfrac{1}{2}\zeta(b-z)^{-\frac{1}{2}}],$$
$$e = \pi^{-\frac{1}{2}}(b-z)^{\frac{1}{2}} \exp[-\tfrac{1}{4}\zeta^2(b-z)^{-1}].$$

The solutions for $j_{r\mathrm{f}}$, $j'_{r\mathrm{f}}$, $\mathrm{j}_{z\mathrm{f}}$ and $j'_{z\mathrm{f}}$ are obtained by substituting the solutions (25) into the equations (21*a*, *c*), by integrating the equation (21*c*) with respect to ζ, and by using the conditions (24*f*) to evaluate the integration functions of z. The solutions for ϕ_f and ϕ'_f are obtained by substituting the equations (21*a*, 25) into the stretched equation (2*f*), by integrating the result with respect to ζ, and by using the conditions

$$\phi_\mathrm{f} \rightarrow a\zeta, \quad \phi'_\mathrm{f} \rightarrow C_2 + \tfrac{1}{2}\zeta^2, \quad \text{as } \zeta \rightarrow \infty,$$

to evaluate the integration functions. Here C_2 is a constant, $O(M^{-1})$ voltage in the outer core which is determined by the value of $\Phi'_\mathrm{i}(a)$.

The solution (25*a*) accommodates the difference between $v_{\theta\mathrm{i}}(a)$ in the inner core and $v_\theta = a$ in the outer core, and it involves exactly the total, $O(M^{-1})$ axial current already assumed in the electric circuit sketched in figure 3. The solution (25*b*) accommodates the difference between $\mathrm{d}v_{\theta\mathrm{i}}/\mathrm{d}r(a)$ in the inner core and $\mathrm{d}v_\theta/\mathrm{d}r = 1$ in the outer core, and it incorporates the effects of the curvature of the free shear layer, which are represented by h'_1 and h'_2. However, this $O(M^{-\frac{1}{2}})$ free-shear-layer solution does not produce an $O(M^{-\frac{1}{2}})$ perturbation in either the inner or outer cores. The solutions for the next terms in the asymptotic expansions for the free shear layer, which would be denoted by double primes, would be governed by precisely the same equations (21) and boundary conditions (22–24) with different expressions for h''_j, for $j = 1$–6. This solution accommodates the difference between $v'_{\theta\mathrm{i}}(a, z)$ and $\mathrm{d}^2v_{\theta\mathrm{i}}/\mathrm{d}r^2(a)$ in the inner core and the corresponding zero values in the outer core, and it completes the electrical circuit for the $O(M^{-2})$ inner-core axial current. This solution is not presented here simply because it is lengthy and not very informative.

4. Isothermal meridional motion

The variables v_r, v_z, j_θ, p, T and $f(r)$ are governed by the equations (2*a*, *c*) with the terms which are multiplied by N^{-1} replaced by zeros, by the equations (2*d*, *g*, *i*), by the boundary conditions (3*a*, *b*, *e*, *f*, 4*a*, *d*, *e*, 5*a*, *b*) and by thermal boundary conditions which will be presented in a future paper. If we assume temporarily that $T(r,z)$ is known then the problem without the equation (2*i*) is a linear problem governing v_r, v_z, j_θ, p and f. The only inhomogeneous terms in this problem are the two body forces, namely the centrifugal force, $-v_\theta^2/r$, in (2*a*) and the buoyancy force, $v_{\mathrm{bc}}T$, in the equation (2*c*). We can solve separately for the meridional motions due to the centrifugal force and due to the buoyancy force, where the former is completely determined since v_θ is now known, while the latter is expressed in terms of integrals of the actually unknown function $T(r,z)$. The two velocities are added together and introduced into (2*i*) to obtain a nonlinear equation involving only one unknown, $T(r,z)$. The expressions for v_r, v_z, j_θ, p and f due to the buoyancy force and the numerical solutions of (2*i*) with the appropriate thermal boundary conditions will be presented in a future paper. Here we present the solutions for the motion due to the centrifugal force, i.e. the isothermal meridional motion for $T = 0$.

In the outer core, vertical wall layer and adjacent Hartmann layers and intersection regions, $v_\theta = r$ to all orders in M. The solutions

$$v_r = v_z = j_\theta = 0, \quad p = \tfrac{1}{2}(r^2 - a^2), \quad f = Fp \qquad (26a\text{–}e)$$

satisfy $(2a, c, d, g)$, with $T = 0$, and the boundary conditions $(3a, b, e, f, 4a, d, e)$ identically, i.e. to all orders in M. Therefore, for $r > a$, the only meridional motion is that due to buoyancy, and the centrifugal force merely produces a radial pressure gradient which deflects the free surface into a parabola.

In the inner core, the variables are written as asymptotic expansions, such as $v_r = v_{r\mathrm{i}} + M^{-1}v'_{r\mathrm{i}} + O(M^{-2})$. The jump in v_z across either Hartmann layer is $O(M^{-1})$, so that the $O(1)$ inner-core solutions which satisfy $(2a, c, d, g)$ and the boundary conditions $(3b, 5b)$ are

$$v_{r\mathrm{i}} = v_{z\mathrm{i}} = j_{\theta\mathrm{i}} = 0, \quad \frac{\mathrm{d}p_\mathrm{i}}{\mathrm{d}r} = \frac{v_{\theta\mathrm{i}}^2}{r}, \tag{27a–d}$$

where $v_{\theta\mathrm{i}}$ is given by (20). The same axial stretching is used for each Hartmann layer, and $v_{r\mathrm{h}}, j_{\theta\mathrm{h}}$ and p_h denote $O(1)$ quantities, while $v_{z\mathrm{h}}$ denotes an $O(M^{-1})$ quantity. The equation $(2c)$ indicates that $p_\mathrm{h} = p_\mathrm{i}(r)$ in both Hartmann layers. The solutions of the stretched equation $(2a)$, with $v_{\theta\mathrm{h}}$ given by either $(11a)$ or $(14c)$ for the bottom or top Hartmann layer, respectively, must also satisfy $(2g)$ and one of the boundary conditions $(3a, 5a)$. The solutions which also match the core solutions (27) are

$$v_{r\mathrm{h}} = -j_{\theta\mathrm{h}} = r^{-1}v_{\theta\mathrm{i}}(r - v_{\theta\mathrm{i}})\,Z\exp(-Z) + \tfrac{1}{3}r^{-1}(r - v_{\theta\mathrm{i}})^2\,[\exp(-Z) - \exp(-2Z)], \tag{28a}$$

$$v_{r\mathrm{h}} = -j_{\theta\mathrm{h}} = -r^{-1}v_{\theta\mathrm{i}}(\epsilon r - v_{\theta\mathrm{i}})\,Z'\exp(Z') + \tfrac{1}{3}r^{-1}(\epsilon r - v_{\theta\mathrm{i}})^2\,[\exp(Z') - \exp(2Z')], \tag{28b}$$

for the Hartmann layers on the crucible bottom for $r < a$ and on the crystal face, respectively.

We introduce the solutions (28) into the stretched equations $(2d)$, and we integrate from $Z = 0$ or $Z' = 0$, where the conditions $(3b, 5b)$ indicate that $v_{z\mathrm{h}} = 0$, to arbitrary Z or Z' in order to obtain the solutions for $v_{z\mathrm{h}}$ in both Hartmann layers. Matching the $O(M^{-1})$ axial velocities in the Hartmann layers and the inner core leads to the boundary conditions

$$v'_{z\mathrm{i}} = -r^{-1}\frac{\mathrm{d}}{\mathrm{d}r}(rQ_\mathrm{c}), \quad \text{at } z = 0, \tag{29a}$$

$$v'_{z\mathrm{i}} = r^{-1}\frac{\mathrm{d}}{\mathrm{d}r}(rQ_\mathrm{s}), \quad \text{at } z = b, \tag{29b}$$

where

$$Q_\mathrm{c} = \int_0^\infty v_{r\mathrm{h}}\,\mathrm{d}Z = \tfrac{1}{6}r^{-1}(r - v_{\theta\mathrm{i}})\,(r + 5v_{\theta\mathrm{i}}), \tag{30a}$$

$$Q_\mathrm{s} = \int_{-\infty}^0 v_{r\mathrm{h}}\,\mathrm{d}Z' = \tfrac{1}{6}r^{-1}(\epsilon r - v_{\theta\mathrm{i}})\,(\epsilon r + 5v_{\theta\mathrm{i}}), \tag{30b}$$

and $v_{r\mathrm{h}}$ in the definitions of Q_c and Q_s are given by the solution $(28a)$ and the solution $(28b)$, respectively. The $O(M^{-1})$ dimensionless volumetric flow rate across the cylinder with radius r is given by $2\pi r\,Q_\mathrm{c}(r)$ or $2\pi r\,Q_\mathrm{s}(r)$ for the Hartmann layer on the crucible bottom for $r < a$ or on the crystal face, respectively.

The $O(M^{-1})$ inner-core centrifugal force in $(2a)$ is $-2v_{\theta\mathrm{i}}v'_{\theta\mathrm{i}}/r$, where $v_{\theta\mathrm{i}}$ and $v'_{\theta\mathrm{i}}$ are given by $(13a, c, 20)$. The $O(M^{-1})$ inner-core variables which satisfy $(2a, c, d, g)$ and the boundary conditions (29) are

$$\frac{\mathrm{d}p'_\mathrm{i}}{\mathrm{d}r} = \frac{v_{\theta\mathrm{i}}}{r}\left[2\frac{\mathrm{d}\Phi'_\mathrm{i}}{\mathrm{d}r} - \frac{b}{a}(1 - \epsilon)\,G\right] + \frac{1}{b}(Q_\mathrm{c} + Q_\mathrm{s}), \tag{31a}$$

$$v'_{r\mathrm{i}} = -j'_{\theta\mathrm{i}} = \frac{a^2}{r}\frac{\partial\psi}{\partial z}, \quad v'_{z\mathrm{i}} = -\frac{a^2}{r}\frac{\partial\psi}{\partial r}, \tag{31b,c}$$

where

$$\psi = \left(\frac{b}{a}\right)^2 (\xi-\xi^2)(1-\epsilon)\left(\frac{v_{\theta \mathrm{i}}}{a}\right) G + (1-\xi)\, R\left(\frac{Q_\mathrm{c}}{a}\right) - \xi R\left(\frac{Q_\mathrm{s}}{a}\right), \tag{32}$$

is a stream function for the $O(M^{-1})$ inner-core meridional motion, while

$$\xi = \frac{z}{b}, \quad G(R) = 3\frac{\mathrm{d}\omega}{\mathrm{d}R} + R\frac{\mathrm{d}^2\omega}{\mathrm{d}R^2}. \tag{33a, b}$$

The functions $v_{\theta \mathrm{i}}/a$, Q_c/a and Q_s/a in the stream function (32) are functions of R which depend on the ratio of rotation rates ϵ and the resistance ratio γ, but which are independent of a and b. Therefore, the only effect of the melt depth is represented by the factor $(b/a)^2$ in (32).

The key to the meridional solutions (26–32) is the axial variation of v_θ. The equation (2c) indicates that p is independent of z in the cores and Hartmann layers, neglecting $O(M^{-2})$ terms. If v_θ is also independent of z, then $\mathrm{d}p/\mathrm{d}r$ can balance the centrifugal force everywhere, and there is no meridional motion. This is the case for the outer- and the $O(1)$ inner-core solutions (26, 27). The $O(1)$ pressure gradient, which balances the centrifugal force due to $v_{\theta \mathrm{i}}$, is continuous across the Hartmann layers, but $v_{\theta \mathrm{h}}$ must vary from $v_{\theta \mathrm{i}}$ to r or ϵr, as represented by the solutions (11a, 14c). Therefore, the $O(1)$ pressure gradient and centrifugal force do not balance in the Hartmann layers, and the difference drives an $O(1)$ radial velocity in each layer, given by the solutions (28). Since this radial velocity is confined to the thin Hartmann layers, it represents an $O(M^{-1})$ volumetric flow rate which is drawn from the inner core and propelled radially outward towards the free shear layer for $Q > 0$, or in the opposite direction for $Q < 0$. The sign of Q_c or Q_s depends on the relative magnitudes of the net effective centrifugal force due to $v_{\theta \mathrm{h}}$ and of the centrifugal force due to $v_{\theta \mathrm{i}}$; when the former exceeds the latter, there is radially outward flow, and $Q > 0$. Since the centrifugal pumping in the Hartmann layers draws fluid from or discharges fluid into the inner-core, there is an $O(M^{-1})$ inner-core meridional flow driven by the Hartmann-layer pumping and represented by the last two terms in the stream function (32).

Since the $O(M^{-1})$ inner-core $v'_{\theta \mathrm{i}}$ varies linearly with z, $\mathrm{d}p'_\mathrm{i}/\mathrm{d}r$ can only balance an axial average of the associated centrifugal force. The difference between the pressure gradient and the local centrifugal force at each elevation drives an $O(M^{-1})$ inner-core meridional flow, which is represented by the first term in the stream function (32). This circulation is symmetric about $z = \frac{1}{2}b$ and vanishes at $z = 0, b$. The inner-core meridional motion driven by its own centrifugal pumping is associated with the axial variation of $v'_{\theta \mathrm{i}}$, and, in the previous section, we saw that this variation is associated with the deviation of $v_{\theta \mathrm{i}}$ from a rigid-body rotation. The function G, given by (33b), is a measure of this deviation and depends only on R and the parameter γ. From figure 5, we see that both terms in G are relatively small for $0.2 < R < 0.7$ for most values of γ. Both terms are larger for $R < 0.2$, but tend to cancel since the first and second derivations of ω are positive and negative, respectively. However, both terms are large and positive for $R > 0.7$, so that the circulation due to the inner-core pumping tends to be concentrated near the free shear layer, $0.7 < R < 1$, coinciding with the large shearing in $v_{\theta \mathrm{i}}$.

In order to develop a complete picture of the isothermal meridional motion for various values of the parameters γ, ϵ and (b/a), we first separate the motions due to the inner-core and Hartmann-layer centrifugal pumping, i.e. we consider the first term and the last two terms in the stream function (32) separately. Plotted separately as functions of R and ξ for $0 \leqslant R, \xi \leqslant 1$, the streamlines for the two motions depend on γ and ϵ, but are independent of (b/a).

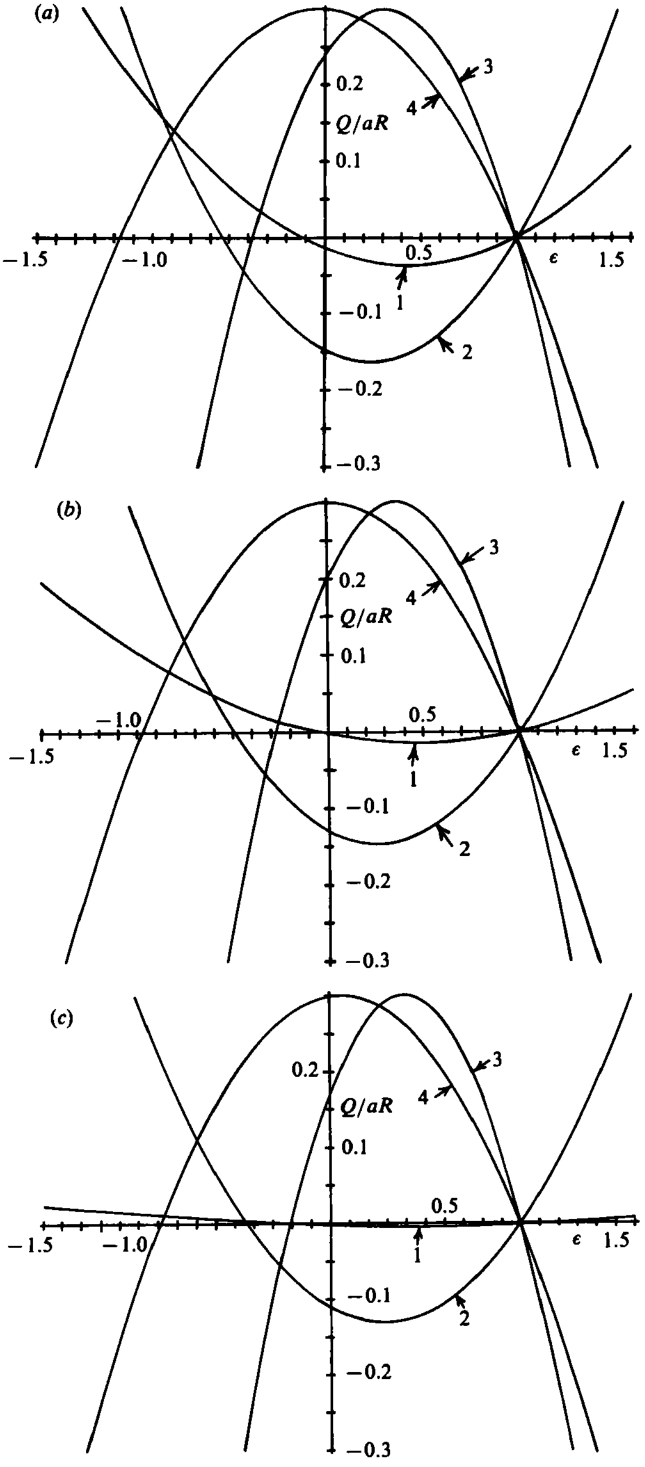

FIGURE 6. The $O(M^{-1})$ radial volumetric flow rate Q in the Hartmann layers. (*a*) $\gamma = 4.643$, (*b*) $\gamma = 8.125$, (*c*) $\gamma = 16.25$. In all three graphs: $1 = (Q_s/aR)$ at $R = 0$, and $2 = (Q_s/aR)$ at $R = 1$, $3 = (Q_c/aR)$ at $R = 0$, and $4 = (Q_c/aR)$ at $R = 1$, where Q_s and Q_c are the flow rates in the Hartmann layers on the crystal face and on the crucible bottom, respectively.

Figure 6 presents graphs of (Q_s/aR) and (Q_c/aR) at $R = 0$ and $R = 1$, as functions of ϵ, the ratio of the crystal's rotation rate to the crucible's, for $\gamma = 4.643$, 8.125 and 16.25 ($B = 0.10$ T, 0.17 T and 0.34 T, for an 8 cm diameter silicon crystal). Since ω increases monotonically with R, the value of (Q/aR) varies monotonically between its values at $R = 0$ and $R = 1$, so that figure 6 indicates qualitatively the magnitude and sign of (Q/a) for both Hartmann layers and for all R.

For $\epsilon > 1$ (co-rotation with faster crystal rotation), $r < v_{\theta i} < \epsilon r$, so that $v_{\theta h} > v_{\theta i}$ in the top Hartmann layer and $Q_s > 0$, while $v_{\theta h} < v_{\theta i}$ in the bottom Hartmann layer and $Q_c < 0$. For $0 < \epsilon < 1$ (co-rotation with slower crystal rotation), $\epsilon r < v_{\theta i} < r$, so that $v_{\theta h} < v_{\theta i}$ in the top Hartmann layer and $Q_s < 0$, while $v_{\theta h} > v_{\theta i}$ in the bottom Hartmann layer and $Q_c > 0$. For a small and negative ϵ (counter-rotation with much slower crystal rotation), the inner core is still dominated by the crucible rotation, so that $0 < v_{\theta i} < \frac{1}{2}r$. In the bottom Hartmann layer, $v_{\theta h} > v_{\theta i}$ and $Q_c > 0$. In the top Hartmann layer, $v_{\theta h}$ varies from $v_{\theta i} > 0$ at $Z' = -\infty$, through zero, to $\epsilon r < 0$ at $Z' = 0$, and this reversal in the azimuthal velocity means that the net centrifugal force is small, so that $Q_s < 0$. The fluid near $R = 0$ tends to rotate with the crystal, while that near $R = 1$ tends to rotate with the average angular velocity. As we increase the crystal rotation rate for counter-rotation, the inner-core fluid near $R = 0$ first ceases to rotate and then begins to rotate in the same direction as the crystal, i.e. $v_{\theta i} < 0$, near $R = 0$. The fluid near the free shear layer is still rotating in the same direction as the crucible, i.e. $v_{\theta i} > 0$, near $R = 1$. In the top Hartmann layer near $R = 0$, $v_{\theta h} < v_{\theta i} < 0$ and $Q_s > 0$. In the bottom Hartmann layer near $R = 0$, $v_{\theta h}$ varies from $v_{\theta i} < 0$, through zero, to $r > 0$, so that now this Hartmann layer has the flow reversal with the associated small centrifugal force, which means that Q_c near $R = 0$ decreases rapidly and becomes negative as ϵ decreases to larger negative values. Near $R = 1$, $v_{\theta i}$ is still positive, so that $v_{\theta h} > v_{\theta i}$ in the bottom Hartmann layer and $Q_c > 0$, while the top Hartmann layer has a flow reversal with $Q_s < 0$. As ϵ decreases further, the radius at which $v_{\theta i} = 0$ increases and eventually the entire inner core is rotating in the same direction as the crystal, i.e. $v_{\theta i} < 0$ for all R. Now, $v_{\theta h} < v_{\theta i} < 0$ throughout the top Hartmann layer and $Q_s > 0$ for all R. Near $R = 0$, $v_{\theta i}$ approaches ϵr, so that $v_{\theta h}$ in the bottom Hartmann layer varies from nearly $\epsilon r < 0$, through zero, to $r > 0$, and the average $v_{\theta h}^2$ is less than $v_{\theta i}^2$, so $Q_c < 0$, near $R = 0$. Near $R = 1$ at the value of ϵ for which $v_{\theta i} = 0$ at $R = 1$, $v_{\theta h}$ in the bottom Hartmann layer increases from $v_{\theta i} = 0$ to r, so that $Q_c > 0$, near $R = 1$. However, as ϵ decreases from this value, the magnitude of the negative $v_{\theta i}$ at $R = 1$ increases, so that $v_{\theta h}$ in the bottom Hartmann layer has a flow reversal with the associated small centrifugal force, which means that Q_c near $R = 1$ decreases rapidly and becomes negative as ϵ decreases. Finally, for $\epsilon < -1.07$, for $\gamma = 4.643$ (counter-rotation with faster crystal rotation), the inner core rotates in the same direction as the crystal ($v_{\theta i} < 0$), $Q_s > 0$, there is a reversal in $v_{\theta h}$ in the bottom Hartmann layer, and $Q_c < 0$, for all R.

Comparison of the graphs in figure 6 for the three different values of γ leads to the surprising conclusion that the results are relatively insensitive to these variations of γ. In other words, Q_s and Q_c, as defined here, are relatively independent of the magnetic field strength for the range of strengths being considered for magnetic Czochralski. However, since the characteristic meridional velocity v_c varies as B^{-2}, and since we are dealing with an $O(M^{-1})$ dimensionless meridional circulation, a constant Q corresponds to a dimensional volumetric flow rate which varies as B^{-3}. Therefore, the actual flows decrease rapidly as the magnetic field strength increases. The curves in figure 6 are all parabolas with one zero at $\epsilon = 1$ (iso-rotation). For any γ and R, (Q_c/aR) has a maximum of 0.3 at a small, positive or slightly negative value of ϵ. The second zero on all four curves moves slightly towards $\epsilon = 0$ as γ increases. The principal effect of increasing γ is to decrease the magnitude of (Q_s/aR) near $R = 0$ for any ϵ. For $\gamma = 16.25$, (Q_s/aR) at $R = 0$ is virtually zero for all ϵ, i.e. there is virtually no radial flow in the top Hartmann layer near $R = 0$ for any rotation rates. As γ increases, $\omega(0)$ approaches zero, so that the rotation of the central column of fluid near $R = 0$ approaches the rotation of the crystal. Therefore, the jump in v_θ across the top Hartmann layer near $R = 0$ approaches zero as γ increases, so that there is no longer an imbalance between the pressure gradient and the centrifugal force to drive a radial flow here.

The last two terms in the stream function (32) represent a linear variation of ψ with ξ from RQ_c/a at $\xi = 0$ to $-RQ_s/a$ at $\xi = 1$. Therefore, we can use the results in figure 6 to sketch the possible streamline patterns for the meridional circulation driven by the Hartmann-layer pumping. For $\epsilon > 1$, the flow is a clockwise circulation around the streamlines sketched in figure 7(*a*). For $\epsilon_1 < \epsilon < 1$, the flow is a counterclockwise circulation around the same streamlines. The specific values of ϵ at which the flow pattern changes are given in table 2 for three values of γ. As ϵ approaches ϵ_1 from above, all the curves in figure 6 are rapidly approaching zero except those for Q_c at $R = 1$, so that the streamlines for $R < 0.5$ disappear and an increasing number of streamlines close through the inner core, bottom Hartmann layer and free shear layer. At $\epsilon = \epsilon_1$, a clockwise circulation near the centre of the crystal face appears, and this circulation grows as ϵ decreases from ϵ_1. The flow pattern for $\epsilon_2 < \epsilon < \epsilon_1$ is sketched in figure 7(*b*). At $\epsilon = \epsilon_2$, the clockwise circulation just touches the crucible bottom at $R = 0$, and its streamlines are drawn into the bottom Hartmann layer near $R = 0$ as ϵ decreases from ϵ_2. The flow pattern for $\epsilon_3 < \epsilon < \epsilon_2$ is sketched in figure 7(*c*). At $\epsilon = \epsilon_3$, the clockwise circulation just reaches the crystal edge at $R = 1$, and its streamlines enter the free shear layer as ϵ decreases from ϵ_3. The flow pattern for $\epsilon_4 < \epsilon < \epsilon_3$ is sketched in figure 7(*d*). At $\epsilon = \epsilon_4$, the counterclockwise circulation near $R = 1$, $\xi = 0$ disappears, leaving only clockwise circulation. The flow pattern for $\epsilon_5 < \epsilon < \epsilon_4$ is sketched in figure 7(*e*). At $R = 1$, the magnitude of Q_s exceeds that of Q_c, so that there is flow from the free shear layer into the inner core. At $\epsilon = \epsilon_5$, the magnitudes of Q_s and Q_c at $R = 1$ are the same, so that there is no flow between the free shear layer and the inner core. For $\epsilon < \epsilon_5$, clockwise circulation around the streamlines in figure 7(*a*) is recovered.

The first term in the stream function (32) represents the meridional circulation driven by the inner-core centrifugal pumping, which is associated with the axial variation of $v'_{\theta i}$. Here $G > 0$ for all R and γ, so that the flow pattern changes as the sign of $v_{\theta i}$ changes. For $\epsilon > 1$, the flow is a clockwise circulation around the streamlines sketched in figure 8(*a*). For $\epsilon_6 < \epsilon < 1$, the flow is a counterclockwise circulation around the same streamlines. At $\epsilon = \epsilon_6$, $v_{\theta i}$ near $R = 0$ becomes negative, and an extremely weak clockwise circulation develops near $R = 0$, as ϵ decreases from ϵ_6. The flow pattern for $\epsilon_7 < \epsilon < \epsilon_6$ is sketched in figure 8(*b*), where the boundary between the two circulations is at the radius where $v_{\theta i} = 0$. At $\epsilon = \epsilon_7$, $v_{\theta i} = 0$ at $R = 1$, and the counterclockwise circulation disappears. The remaining clockwise circulation is weak everywhere because G is small for $R < 0.7$ and $v_{\theta i}$ is small for $R > 0.7$. The streamlines for $\epsilon_8 < \epsilon < \epsilon_7$ are sketched in figure 8(*c*). As ϵ decreases from ϵ_7, the magnitude of $v_{\theta i}$ at $R = 1$ again becomes significant and its effect is magnified by the large value of G near $R = 1$. Therefore, a slight decrease in ϵ from ϵ_7 draws all the streamlines into the free shear layer and again establishes the strong clockwise circulation near $R = 1$. Thus ϵ_8 is only slightly less than ϵ_7, and the flow is again clockwise circulation around the streamlines in figure 8(*a*) for $\epsilon < \epsilon_8$.

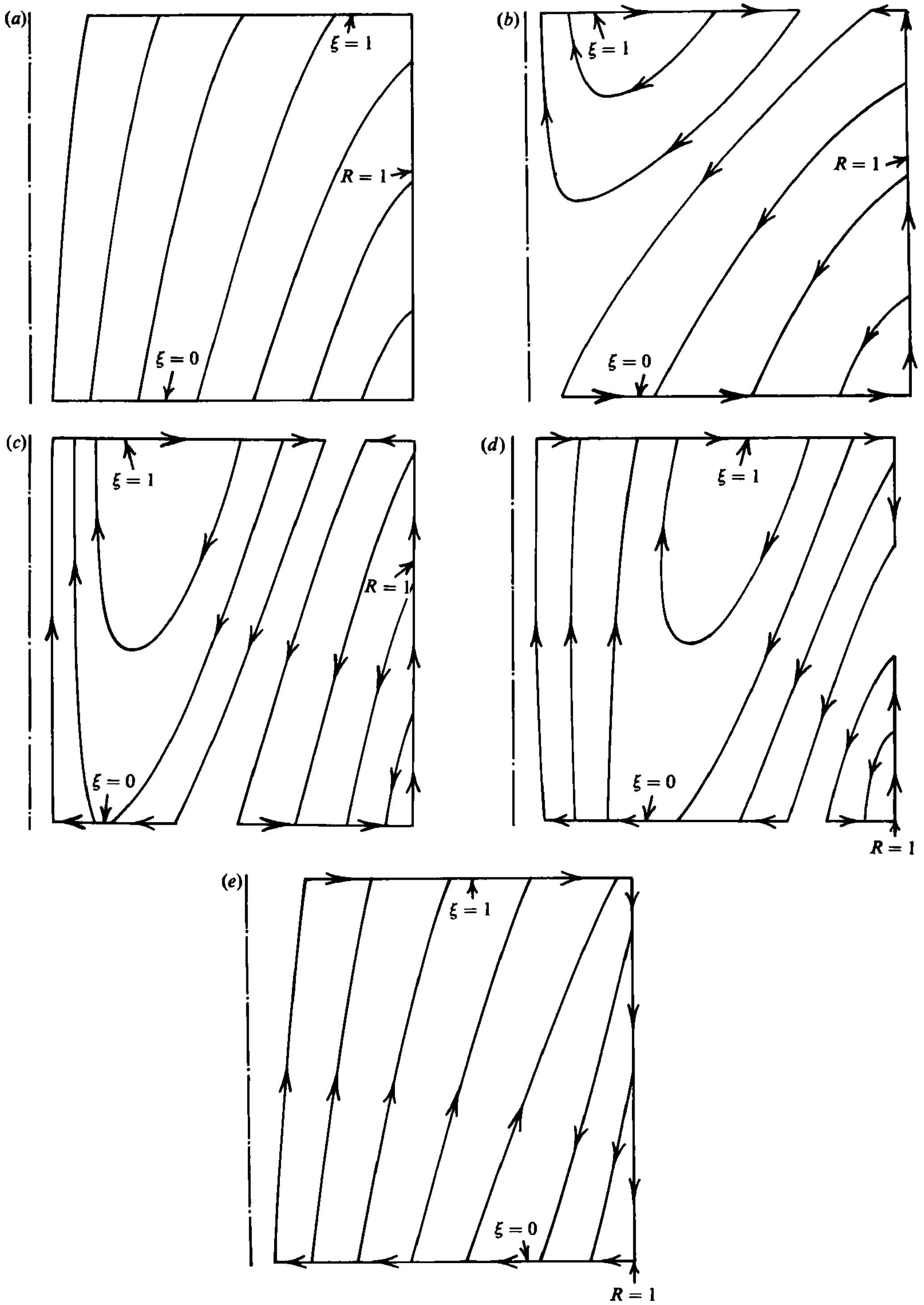

FIGURE 7. Sketches of the streamlines for the meridional motion driven by the Hartmann-layer pumping. The lines at $\xi = 0$ and at $\xi = 1$ represent radial flow in the Hartmann layers on the crucible bottom and on the crystal face, respectively, while the lines at $R = 1$ represent axial flow in the free shear layer. (*a*) $\epsilon > 1$ (clockwise circulation), $\epsilon_1 < \epsilon < 1$ (counterclockwise circulation) and $\epsilon < \epsilon_5$ (clockwise circulation), (*b*) $\epsilon_2 < \epsilon < \epsilon_1$, (*c*) $\epsilon_3 < \epsilon < \epsilon_2$, (*d*) $\epsilon_4 < \epsilon < \epsilon_3$ and (*e*) $\epsilon_5 < \epsilon < \epsilon_4$.

	$\gamma = 4.643$	$\gamma = 8.125$	$\gamma = 16.25$
ϵ_1	-0.1226	-0.0499	-0.0059
ϵ_2	-0.3809	-0.2725	-0.2085
ϵ_3	-0.5404	-0.4870	-0.4371
ϵ_4	-1.0725	-0.9769	-0.8898
ϵ_5	-25.04	-4.006	-2.291
ϵ_6	-0.1507	-0.0604	-0.0070
ϵ_7	-0.7271	-0.6474	-0.5748

TABLE 2. Values of the crystal–crucible rotation ratio at which the flow pattern changes (see figures 7 and 8)

Since oxygen enters the melt from the crucible, and since the diffusion of oxygen in silicon is extremely weak, the two-cell circulation in figure 7(*b*) may prevent oxygen-rich fluid from reaching at least the centre of the crystal face. To protect as much of the crystal as possible, we want to reduce ϵ as much as possible, without causing the clockwise circulation cell to reach the crucible, i.e. we want ϵ slightly more than ϵ_2. Therefore, we choose $\epsilon = -0.38$ for $\gamma = 4.643$ as the example to illustrate the superposition of the meridional motions driven by the Hartmann-layer and inner-core centrifugal pumping. The streamlines for this case and for three different melt depths are presented in figure 9. Since we now have values of b/a, the streamlines are plotted with the proper ratio between the axial and radial scales. In figure 9(*a*), $b/a = 0.5$, which corresponds to a late stage in the growth of a crystal (melt depth = 2 cm for an 8 cm diameter crystal). Since $(b/a)^2 = 0.25$, the contribution of the inner-core pumping is very small, and the flow pattern is primarily due to the Hartmann-layer pumping. The steps in ψ for $\psi > 0$ are ten times those for $\psi < 0$, so that the streamlines above the $\psi = 0$ line represent an extremely weak clockwise circulation under the crystal face, out to $R = 0.827$. Less than a quarter of the flow in the bottom Hartmann layer reaches the crystal face near $R = 1$, while the rest circulates through the free shear layer and inner core.

Going backward through the growth of a crystal to the earlier stage when $b/a = 1.0$, we have the streamlines given in figure 9(*b*). The principal effect of the now stronger inner-core pumping is the addition of a streamline ($\psi = 0.28$) closing entirely through the inner core and free shear layer. The addition of this streamline pushes the other streamlines away from the free shear layer and raises the points where the streamlines $\psi = 0.08$ to 0.24 leave the free shear layer. For $\epsilon = -0.38$ and $\gamma = 4.643$, $v_{\theta i} = 0$ at $R = 0.62$, so that there is a weak clockwise circulation for $R < 0.62$ due to the inner-core pumping. For $b/a = 1.0$, this circulation pulls the negative streamlines down very slightly.

Going to an even earlier stage in the crystal growth when $b/a = 2.0$, we have the streamlines given in figure 9(*c*). The inner-core pumping more than doubles the counterclockwise circulation near $R = 1$, with the streamlines for $\psi = 0.3$ to 0.6 closing through the inner core and free shear layer, and with the streamlines for $\psi = 0.06$ to 0.24 all leaving the free shear layer near the top. The effect of the weak circulation for $R < 0.62$ is to pull the streamlines for $\psi = -0.002$ to -0.006 far down towards the bottom, but not to increase the clockwise circulation here.

The streamlines for $\gamma = 8.125$ with $\epsilon = -0.27$ or for $\gamma = 16.25$ with $\epsilon = -0.20$, and for $b/a = 0.5$, 1.0, 2.0, look very much like those presented in figure 9, except that the weak clockwise circulation above the $\psi = 0$ line becomes even weaker as γ increases with ϵ slightly above ϵ_2 and virtually disappears for $\gamma = 16.25$.

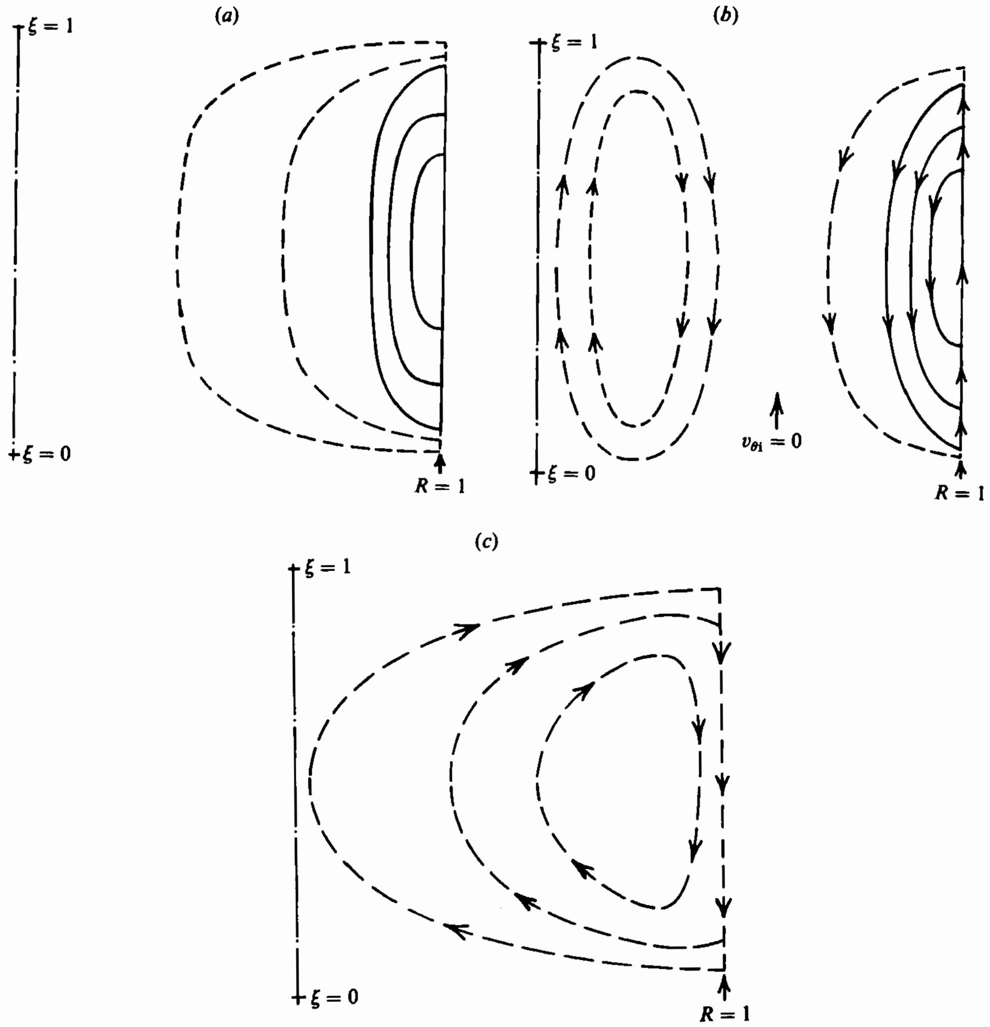

FIGURE 8. Sketches of the streamlines for the meridional motion driven by the inner-core pumping. The lines at $R = 1$ represent axial flow in the free shear layer. (a) $\epsilon > 1$ (clockwise circulation), $\epsilon_6 < \epsilon < 1$ (counterclockwise circulation) and $\epsilon < \epsilon_8$ (clockwise circulation), (b) $\epsilon_7 < \epsilon < \epsilon_6$ and (c) $\epsilon_8 < \epsilon < \epsilon_7$. Dashed lines represent weaker circulation than solid lines.

The great importance of the electrical conductivity of the crystal is revealed by contrasting the correct streamlines in figure 9(c) with the corresponding, erroneous streamlines in figure 10(a) for a crystal which is an electrical insulator. If we erroneously take $\sigma_s = 0$, then $\omega = 0.5$, and $v_{\theta i} = \frac{1}{2}r(1+\epsilon)$. The inner core rotates as a rigid body with the average of the angular velocities of the crystal and crucible. There is no centrifugal pumping in the inner core, because there is no shear in the azimuthal motion here, and $G(R) = 0$ in (32). The inner-core motion is driven entirely by the centrifugal pumping in the Hartmann layers. With the correct value of σ_s, the inner core is more synchronized with the crystal rotation rate, so the insulating crystal solution underestimates the jump in v_θ across the Hartmann layer on the crucible bottom and overestimates this jump across the Hartmann layer on the crystal face, with corresponding errors in the amount of centrifugal pumping in these

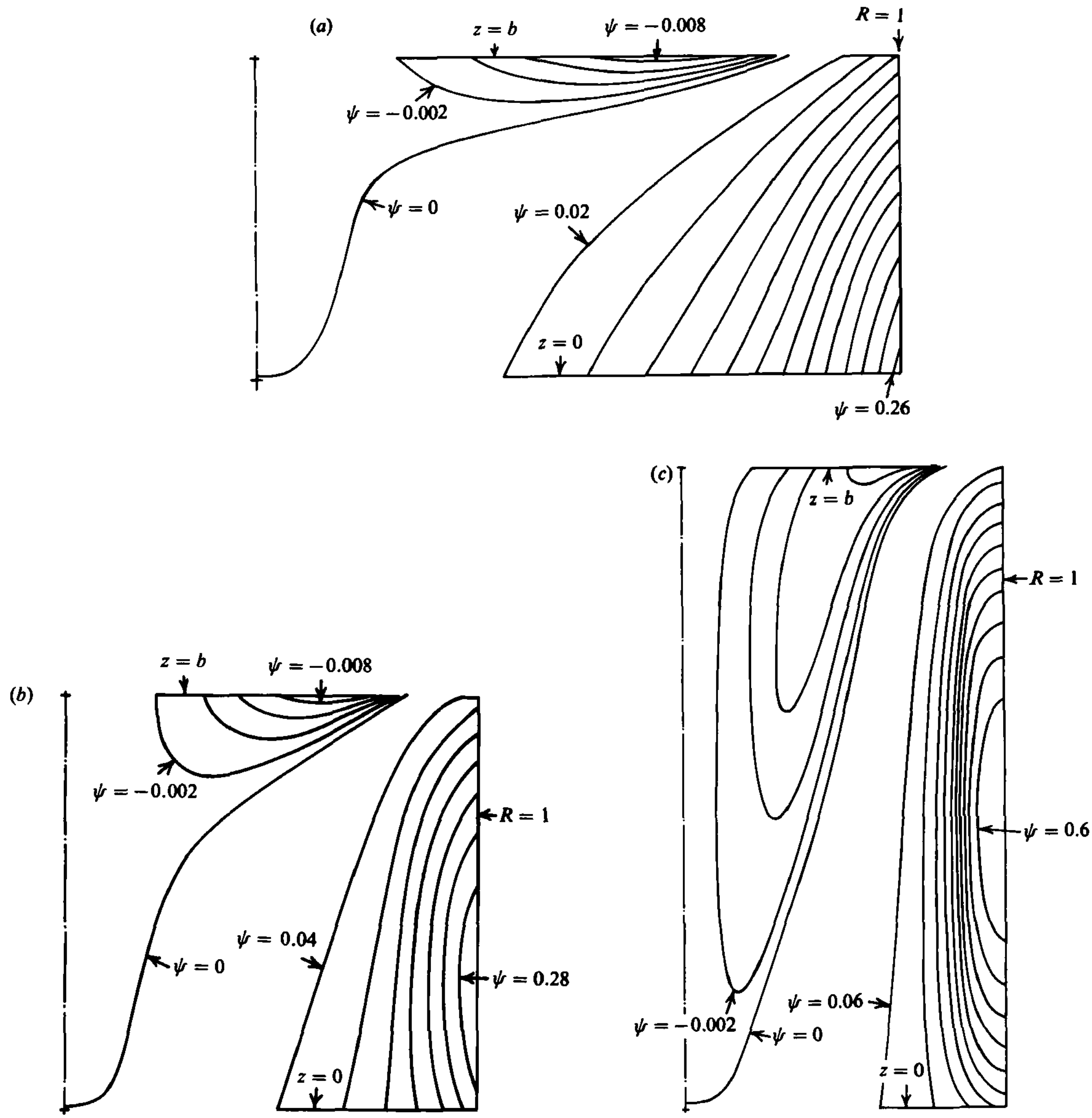

FIGURE 9. Streamlines for $\gamma = 4.643$ and $\epsilon = -0.38$. The lines at $z = 0$ and at $z = b$ represent radial flows in the Hartmann layers on the crucible bottom and on the crystal face, respectively, while the lines at $R = 1$ represent axial flow in the free shear layer. In all three figures, streamlines above the $\psi = 0$ line correspond to $\psi = -0.002k$, for $k = 1$–4, and represent clockwise circulation. Streamlines below and to the right of the $\psi = 0$ line represent counterclockwise circulation with positive values of ψ which are different for each figure. (*a*) $b/a = 0.5$ with positive values of $\psi = 0.02k$, for $k = 1$–13, (*b*) $b/a = 1.0$ with positive values of $\psi = 0.04k$, for $k = 1$–7, and (*c*) $b/a = 2.0$ with positive values of $\psi = 0.06k$, for $k = 1$–10.

layers. These errors are evident in the contrast between the streamlines in figures 9(*c*) and 10(*a*). The role of the crystal conductivity is further illustrated by the streamlines for counter-rotation with equal angular velocities ($\epsilon = -1$). Figure 10(*b*) presents the correct streamlines for $\gamma = 4.643$ and $b/a = 2.0$, while figure 10(*c*) presents the corresponding, incorrect streamlines for an insulating crystal ($\gamma = 0$) and $b/a = 2.0$.

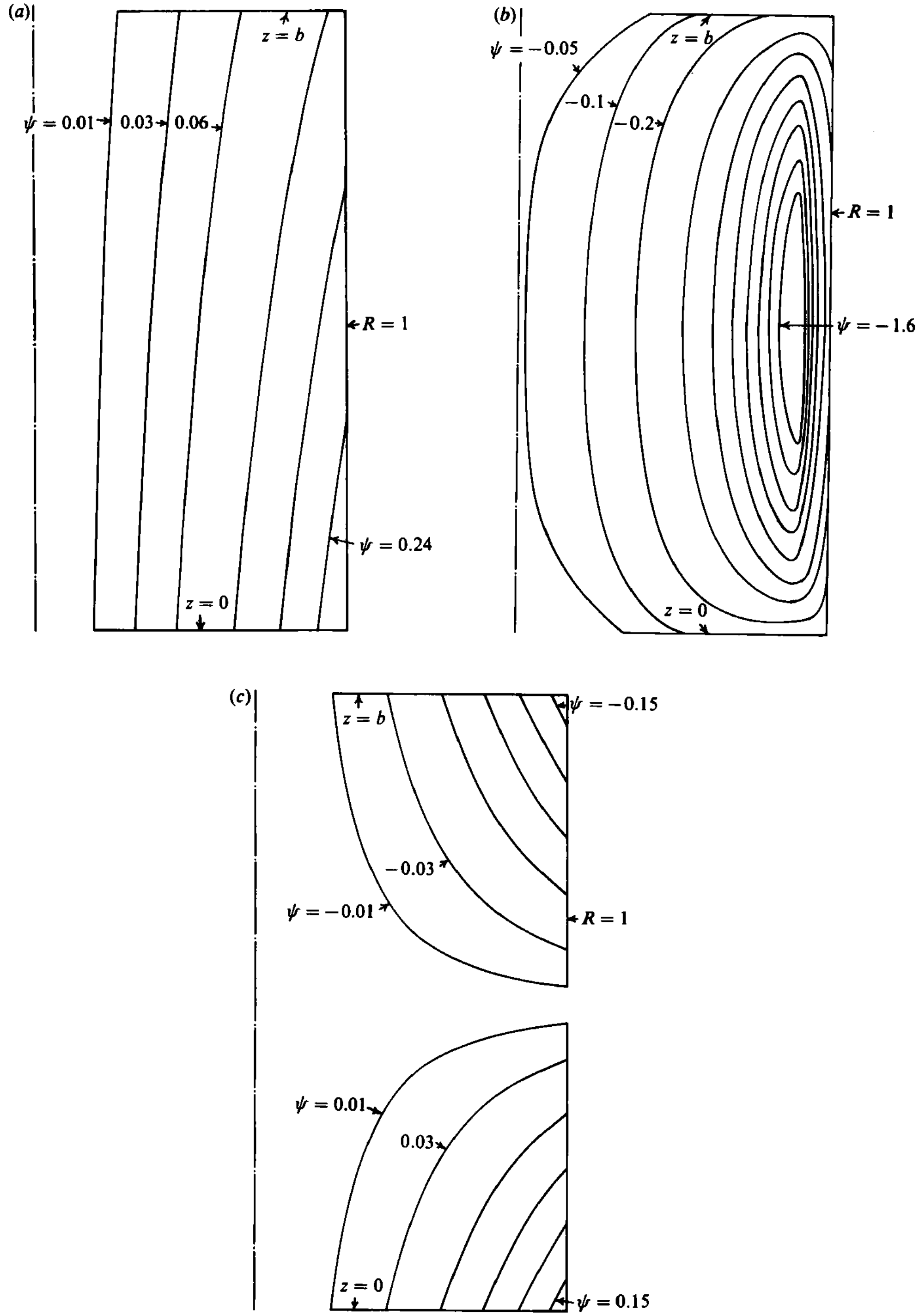

FIGURE 10. Streamlines for $b/a = 2.0$. The lines at $z = 0$ and at $z = b$ represent radial flows in the Hartmann layers on the crucible bottom and on the crystal face, respectively, while the lines at $R = 1$ represent axial flow in the free shear layer. (a) $\gamma = 0$ ($\sigma_s = 0$) and $\epsilon = -0.38$. $\psi = 0.01$, 0.03 and $0.06k$, for $k = 1$–4. (b) $\gamma = 4.643$ and $\epsilon = -1.0$. $\psi = -0.05$, -0.1 and $-0.2k$, for $k = 1$–8. (c) $\gamma = 0$ ($\sigma_s = 0$) and $\epsilon = -1.0$. $\psi = \pm 0.01$ and $\pm 0.03k$, for $k = 1$–5.

Several previous papers present similarity solutions for the flow in a half space of an electrically conducting fluid bounded by an infinite, rotating wall, with a uniform magnetic field applied perpendicular to the wall. For example, Kakutani (1962) presents the solutions for such flows for an electrically insulating wall. Conservation of mass and of electrical charge in the half space occupied by the fluid imply that both the axial velocity and the excess charge are independent of the radial coordinate. This radial uniformity reduces the governing boundary-value problem to a set of equations which admit similarity solutions for the flow field.

If the rotating, insulating wall is replaced by a rotating wall with some electrical conductivity, then the solution to the problem governing the electrical potential function in the wall requires a radial variation which does not vanish at the interface of the wall and the fluid. Since the electrical potential function must be continuous at this interface, the excess electrical charge in the fluid can no longer be independent of the radius. Indeed for an infinite wall, the continuity of electrical potential implies that either the excess charge in the fluid becomes unbounded as the radial distance from the axis increases or that all the fluid, even that infinitely far from the wall, rotates as a rigid body with the wall. Both possibilities are physically unreasonable.

The similarity solution for an infinite, rotating wall is intended to approximate the flow in some small neighbourhood of the axis of rotation for a rotating wall with finite radius. This approximation is valid if a change in a variable at a large radius has negligible effect on the variables at small radius. In fluid dynamics, this is frequently true. However, for electrical variables, this is more often not the case. Electrical problems involve complete electrical circuits with the electrical current and voltage at any point dependent on the entire circuit. With an infinite, rotating, electrically conducting wall with a perpendicular magnetic field, the electric field in the wall increases with radius. Thus the enormous electrical field at large radius totally overwhelms the variables at small radius, giving a completely different flow at small radius than that for a wall with a finite radius. For rotating, electrically conducting walls, the outside radius is important, no matter how much larger it is than the boundary-layer thickness. The electrical potential and excess charge in the fluid are coupled to the variables in the wall and the excess charge must vary radially. Since the outside radius is always important, physically relevant similarity solutions are not possible.

5. Meridional motion in the free shear layer

For the free shear layer, we introduce the same radial stretching, $\zeta = M^{\frac{1}{2}}(r-a)$, and the asymptotic expansions

$$v_z = M^{\frac{1}{2}}v_{z\mathrm{f}} + v'_{z\mathrm{f}} + M^{-\frac{1}{2}}v''_{z\mathrm{f}} + O(M^{-1}), \quad v_r = v_{r\mathrm{f}} + M^{-\frac{1}{2}}v'_{r\mathrm{f}} + M^{-1}v''_{r\mathrm{f}} + O(M^{-\frac{3}{2}}),$$

$$j_\theta = j_{\theta\mathrm{f}} + M^{-\frac{1}{2}}j'_{\theta\mathrm{f}} + M^{-1}j''_{\theta\mathrm{f}} + O(M^{-\frac{3}{2}}), \quad p = M^{-\frac{1}{2}}p_\mathrm{f} + M^{-1}p'_\mathrm{f} + M^{-\frac{3}{2}}p''_\mathrm{f} + O(M^{-2}).$$

With the terms multiplied by N^{-1} replaced by zeros and with $T = 0$ for the isothermal motion, $(2a, c, d, g)$ become

$$\frac{\partial p_\mathrm{f}}{\partial \zeta} + v_{r\mathrm{f}} = H_1, \quad \frac{\partial v_{r\mathrm{f}}}{\partial \zeta} + \frac{\partial v_{z\mathrm{f}}}{\partial z} = H_2, \tag{34a, b}$$

$$\frac{\partial p_\mathrm{f}}{\partial z} - \frac{\partial^2 v_{z\mathrm{f}}}{\partial \zeta^2} = H_3, \quad j_{\theta\mathrm{f}} = -v_{r\mathrm{f}}, \tag{34c, d}$$

and the same equations with a prime or a double prime added to each variable. Here

$$H_1 = \frac{v_{\theta f}^2}{a}, \quad H_1' = \frac{2v_{\theta f}\, v_{\theta f}'}{a} - \frac{\zeta v_{\theta f}^2}{a^2}, \quad H_1'' = \frac{\partial^2 v_{rf}}{\partial \zeta^2} + \frac{(v_{\theta f}')^2}{a} + \frac{2v_{\theta f}\, v_{\theta f}''}{a} - \frac{2\zeta v_{\theta f}\, v_{\theta f}'}{a^2} + \frac{\zeta^2 v_{\theta f}^2}{a^3},$$

$$H_2 = H_3 = 0, \quad H_2' = -\frac{v_{rf}}{a}, \quad H_2'' = -\frac{v_{rf}'}{a} + \frac{\zeta v_{rf}}{a^2},$$

$$H_3' = a^{-1}\frac{\partial v_{zf}}{\partial \zeta}, \quad H_3'' = a^{-1}\frac{\partial v_{zf}'}{\partial \zeta} + \frac{\partial^2 v_{zf}}{\partial z^2} - \zeta a^{-2}\frac{\partial v_{zf}}{\partial \zeta}.$$

Matching the outer-core solution (26) gives the boundary conditions

$$v_{zf} \to 0, \quad v_{rf} \to 0, \quad p_f \to H_4, \quad \text{as } \zeta \to \infty, \tag{35}$$

and the same conditions with a prime or double prime added to each variable. Here

$$H_4 = a\zeta, \quad H_4' = \tfrac{1}{2}\zeta^2, \quad H_4'' = 0.$$

Matching the inner-core solutions (27, 31, 32) gives the boundary conditions

$$v_{zf} \to 0, \quad v_{rf} \to H_5, \quad p_f \to H_6, \quad \text{as } \zeta \to -\infty, \tag{36}$$

and the same conditions with a prime or double prime added to each variable. This matching also gives $p_i(a) = 0$, which determines the constant of integration when (27*d*) is integrated. Here

$$H_5 = H_5' = 0, \quad H_5'' = v_{ri}'(a, z),$$

$$H_6 = C_3 + \zeta \frac{\mathrm{d}p_i}{\mathrm{d}r}(a), \quad H_6' = p_i'(a) + \tfrac{1}{2}\zeta^2 \frac{\mathrm{d}^2 p_i}{\mathrm{d}r^2}(a), \quad H_6'' = C_4 + \zeta \frac{\mathrm{d}p_i'}{\mathrm{d}r}(a) + \tfrac{1}{6}\zeta^3 \frac{\mathrm{d}^3 p_i}{\mathrm{d}r^3}(a),$$

where C_3 and C_4 represent $O(M^{-\frac{1}{2}})$ and $O(M^{-\frac{3}{2}})$ constant pressures in the inner core, while C_3, C_4 and $p_i'(a)$ are determined as parts of the free-shear-layer solutions. The actual inner-core pressure is

$$p = p_i(r) + M^{-\frac{1}{2}}C_3 + M^{-1}p_i'(r) + M^{-\frac{3}{2}}C_4 + O(M^{-2}),$$

but there are no $O(M^{-\frac{1}{2}})$ or $O(M^{-\frac{3}{2}})$ inner-core velocities, electric currents or electric potentials.

The $O(1)$ radial velocity in the intersection region at $r = a$ on the crucible bottom is given by the term

$$v_{rf}(\zeta, 0)\,[1 - \exp(-Z)],$$

plus the expression (28*a*) with r and $v_{\theta i}$ replaced by a and $v_{\theta f}(\zeta, 0)$, respectively. With this solution, with both radial and axial stretching, with integration across the intersection region and with the boundary condition (3*b*), (2*d*) gives the boundary conditions

$$v_{zf}'' = \frac{\partial v_{rf}}{\partial \zeta} - \frac{\partial v_{\theta f}}{\partial \zeta}\,\frac{2a - 5v_{\theta f}}{3a}, \tag{37a}$$

$$v_{zf} = v_{zf}' = 0, \quad \text{at } z = 0, \tag{37b,c}$$

for all ζ. The $O(1)$ radial velocity in the intersection region on the crystal face is given by the term

$$v_{rf}(\zeta, b)\,[1 - \exp(Z')],$$

plus (28*b*) evaluated at $r = a$, because the solution (25*a*) gives $v_{\theta f}(\zeta, b) = v_{\theta i}(a)$, for $\zeta < 0$. Now (2*d*) and the boundary condition (5*b*) give the boundary conditions

$$v_{zf} = v_{zf}' = 0, \quad v_{zf}'' = -\frac{\partial v_{rf}}{\partial \zeta}, \quad \text{at } z = b, \quad \text{for } \zeta < 0. \tag{38a–c}$$

For the intersection region at $r = a$ on the free surface, the jumps in normal velocity and pressure are $O(M^{-\frac{3}{2}})$ and $O(M^{-2})$, respectively (Hays & Walker 1984), so that the boundary conditions $(4a, e)$ can be applied directly to the present asymptotic solutions for the free shear layer. Since p varies through the free shear layer, the free surface is deflected to the position

$$z = b + M^{-\frac{1}{2}} f_{\mathrm{f}}(\zeta) + M^{-1} f'_{\mathrm{f}}(\zeta) + O(M^{-\frac{3}{2}}),$$

where the boundary condition $(4e)$ gives

$$f_{\mathrm{f}} = Fp_{\mathrm{f}}(\zeta, b), \quad f'_{\mathrm{f}} = Fp'_{\mathrm{f}}(\zeta, b) + Ff_{\mathrm{f}} \frac{\partial p_{\mathrm{f}}}{\partial z}(\zeta, b).$$

The boundary condition $(4a)$ gives the boundary conditions

$$v''_{z\mathrm{f}} = a^{-1} f_{\mathrm{f}} v_{r\mathrm{f}} + \frac{\partial}{\partial \zeta}\left(f'_{\mathrm{f}} v_{r\mathrm{f}} + f_{\mathrm{f}} v'_{r\mathrm{f}} + \tfrac{1}{2} f_{\mathrm{f}}^2 \frac{\partial v_{r\mathrm{f}}}{\partial z}\right), \tag{39a}$$

$$v_{z\mathrm{f}} = 0, \quad v'_{z\mathrm{f}} = \frac{\partial}{\partial \zeta}(f_{\mathrm{f}} v_{r\mathrm{f}}), \quad \text{at } z = b, \tag{39b, c}$$

for $\zeta > 0$, and for $F = O(1)$. If $F = O(M^{-\frac{1}{2}})$, then $v'_{z\mathrm{f}} = 0$ at $z = b$, and $v''_{z\mathrm{f}}$ is given by the condition $(39c)$.

For the unprimed variables, we introduce the streamfunction $\Psi(\zeta, z)$, where

$$v_{r\mathrm{f}} = -j_{\theta\mathrm{f}} = \frac{\partial \Psi}{\partial z}, \quad v_{z\mathrm{f}} = -\frac{\partial \Psi}{\partial \zeta}. \tag{40a, b}$$

When we introduce $(34c, 40)$ into the z-derivative of $(34a)$, we obtain the equation

$$\frac{\partial^2 \Psi}{\partial z^2} - \frac{\partial^4 \Psi}{\partial \zeta^4} = \frac{\partial H_1}{\partial z}. \tag{41}$$

The boundary conditions $(35, 36, 37b, 38a, 39b)$ become

$$\Psi \to 0 \quad \text{as } \zeta \to \pm\infty; \quad \Psi = 0 \quad \text{at } z = 0, b. \tag{42}$$

Since H_1 involves $v_{\theta 1}(a)$, it depends on the parameters γ and ϵ. However, if we introduce

$$\Psi = \frac{1}{4a}(a^2 - v_{\theta 1}^2)\, \Psi_1 + \frac{1}{4a}(a - v_{\theta 1})^2\, \Psi_2, \tag{43}$$

where $v_{\theta 1}$ is evaluated at $r = a$, then each function Ψ_1 or Ψ_2 is governed by (41) with $\partial H_1/\partial z$ replaced by the term $\zeta e/(b-z)^2$ times one or E, respectively, and by the boundary conditions (42). Therefore, Ψ_1 and Ψ_2 are functions of ζ and z which depend only on the parameter b. The solutions are

$$\Psi_1 = b \sum_{k=0}^{\infty} [\lambda_k(-z) - \lambda_{k+1}(z)] - (b-z)\,\lambda_0(z), \tag{44}$$

where
$$\lambda_k(z) = \mathrm{erf}\,[\tfrac{1}{2}\zeta(2kb + b - z)^{-\frac{1}{2}}],$$

and
$$\Psi_2 = \int_0^z \Lambda_{-1}(z)\,\mathrm{d}z^* + \sum_{k=0}^{\infty} \int_0^b [\Lambda_k(z) - \Lambda_k(-z)]\,\mathrm{d}z^*, \tag{45}$$

where

$$\Lambda_k(z) = -\pi^{-\frac{1}{2}} \zeta q_1 q_2^{-\frac{3}{2}}\, \mathrm{erf}\,(\tfrac{1}{2}\zeta q_1^{\frac{1}{2}} q_2^{-\frac{1}{2}} q_3^{-\frac{1}{2}}) \exp(-\tfrac{1}{4}\zeta^2 q_2^{-1}) - 2\pi^{-1} q_1^{\frac{1}{2}} q_3^{\frac{1}{2}} q_2^{-1} \exp(-\tfrac{1}{2}\zeta^2 q_3^{-1}),$$

$$q_1 = b - z^*, \quad q_2 = 2kb + 3b + z - 2z^*, \quad q_3 = 2q_2 - q_1.$$

The velocities and the electric current are obtained by substituting the solutions (43–45) into (40). The pressure is obtained by introducing (40a) into (34a), by integrating the latter with respect to ζ and by using the condition (35) to determine the function of integration.

The key to the solutions (43–45) is again the axial variation of v_θ, which is represented in (41) by $\partial H_1/\partial z$. In the free shear layer, $v_{\theta f}$ varies from $v_{\theta i}(a)$ at $\zeta = -\infty$ to a at $\zeta = \infty$ for every value of z, but the solution (25a) accommodating this jump involves a $v_{\theta f}$ which is constant along the parabolas $\zeta = C_5(b-z)^{\frac{1}{2}}$, for different values of the constant C_5. In particular, if we define the edges of the free shear layer as the points at which $v_{\theta f}$ deviates from the adjacent core values by 1 % of the total jump, then the edges are at $\zeta = \pm 4.66(b-z)^{\frac{1}{2}}$. Near $z = b$, the layer thickness is small and the jump occurs over a small radial distance but, near $z = 0$, the layer thickness is large and the jump occurs over a large radial distance. In order to illustrate the effects of this axial variation on the centrifugal force, we take $v_{\theta i}(a) = -a$, although the argument is true for any $v_{\theta i}(a)$. For our special example, $v_{\theta f}$ near $z = b$ is equal to $a\,\mathrm{sgn}\,(\zeta)$ everywhere except near $\zeta = 0$, where it accommodates the jump with a large velocity gradient. Therefore, $v_{\theta f}^2 = a^2$ for all values of ζ except very near $\zeta = 0$, and the net centrifugal force near $z = b$ is large. Near $z = 0$, $v_{\theta f}$ deviates from $a\,\mathrm{sgn}\,(\zeta)$ for a long distance on either side of $\zeta = 0$ and accommodates the jump with a very gradual transition. Therefore $v_{\theta f}^2 < a^2$ over a large distance near $\zeta = 0$, and the net centrifugal force near $z = 0$ is small. The pressure difference across the free shear layer is independent of z, because the pressures in both cores are independent of z, so the pressure difference can only balance an axial average of the net centrifugal force. Near $z = b$, the net centrifugal force is larger than the pressure difference, and there is a positive net radial force. Near $z = 0$, the net centrifugal force is smaller than the pressure difference, and there is a negative net radial force. This imbalance drives a clockwise circulation entirely inside the free shear layer, i.e. outward flow near the crystal edge and inward flow near the crucible bottom with the streamlines confined to the layer.

The solution form (43) indicates that the details of the meridional circulation in the free shear layer depend upon ϵ and γ. However, we can extract certain global characteristics of this circulation without knowing the solutions (43–45). We introduce the expressions (20, 25a, 40a) into (34a), we integrate the latter from $\zeta = -\infty$ to $\zeta = \infty$, using the conditions (35, 36) to evaluate p_f here, and we integrate again with respect to z. The boundary conditions (42) at $z = 0, b$ then determine the constant of integration for the second, indefinite integral, and C_3, which is the $O(M^{-\frac{1}{2}})$ inner-core constant pressure balancing the axial average of the net centrifugal force in the free shear layer. The results are

$$C_3 = \tfrac{1}{3}(2)^{\frac{3}{2}}\pi^{-\frac{1}{2}}b^{\frac{1}{2}}a(1-\epsilon)^2[1-\omega(1)]^2, \tag{46a}$$

$$\int_{-\infty}^{\infty} \Psi(\zeta, z)\,\mathrm{d}\zeta = C_3\, b[(1-\xi)^{\frac{3}{2}} - (1-\xi)], \tag{46b}$$

where $\xi = z/b$, as before. The inner-core pressure C_3 is always positive. Consider a fictitious pressure distribution based on H_4 and H_6,

$$\left.\begin{aligned} p_f &= (\zeta/a)(v_{\theta i}(a))^2 \quad \text{for } \zeta < 0, \\ p_f &= a\zeta \quad \text{for } \zeta > 0, \end{aligned}\right\} \tag{47}$$

which would exactly balance the centrifugal force associated with a fictitious velocity, $v_{\theta f} = v_{\theta i}(a)$, for $\zeta < 0$, and $v_{\theta f} = a$, for $\zeta > 0$. However, the actual $v_{\theta f}$ is more gradual

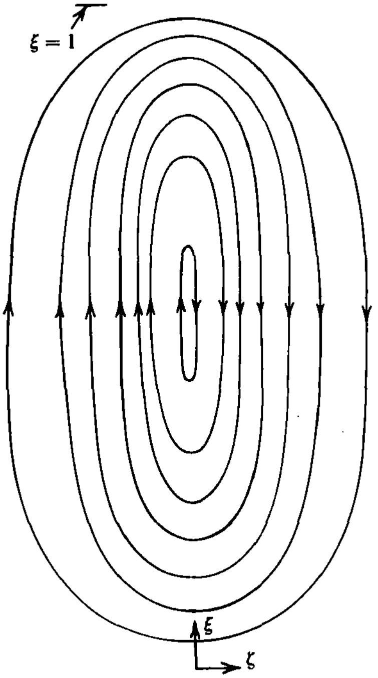

FIGURE 11. Sketch of the streamlines for the $O(1)$ meridional circulation in the free shear layer.

than this step change in azimuthal velocity, so that the net centrifugal force is less. Therefore, the step change in pressure gradient (47) provides too much net radially inward pressure force, and C_3 is the increase in the inner-core pressure needed to maintain overall balance with the actual centrifugal force.

The expression (46*b*) represents a radial average of the streamfunction at each ξ and suggests the streamlines sketched in figure 11. The expression (46*b*) has been used to estimate the locations of the streamlines at $\zeta = 0$. The centre of the circulation is slightly above the middle at $\xi = 0.555$. Streamlines of this form in a radially thin region beneath the crystal edge are evident in the figures 1 (*b*, *c*) presented by Langlois & Lee (1983). The details of this circulation are provided by the solutions (43–45) for different values of ϵ, γ and b, but figure 11 and the expressions (46) provide a rough picture of how the free-shear-layer circulation varies with these parameters. The circulation is clockwise for every situation. The value of $\omega(1)$ depends only on γ. Therefore, a graph of the total volumetric flow rate in this circulation as a function of ϵ is a simple parabola with zero flow at $\epsilon = 1$ (iso-rotation) and increases rapidly as ϵ changes from 1 in either direction. As B increases, $\omega(1)$ decreases from 0.5 to 0, so that C_3 increases. However, a constant, $O(1)$, dimensionless flow rate represents an actual flow rate which varies as B^{-2}. Therefore the actual flow rate varies as $[1-\omega(1)]^2B^{-2}$. For example, relative to the actual flow rate for $\gamma = 4.643$, those for $\gamma = 8.125$ and 16.25 are 0.359 and 0.0979, respectively, for the same ϵ and b. The expression (46*b*) suggests that the flow rate varies as $b^{\frac{3}{2}}$, so the free-shear-layer circulation decreases as the crystal is grown, and the melt depth decreases.

The solutions (43–45) represent a meridional circulation inside the free shear layer with an $O(1)$ dimensionless flow rate, while the solutions (30–32) represent a meridional circulation through the inner core, Hartmann layers and free shear layer with an $O(M^{-1})$ flow rate. The former circulation involves a much larger flow rate than the latter. However, the former involves circulation only inside the free shear layer, so that its only direct transport from the crucible to the crystal is at the crystal edge, where evaporation from the adjacent free surface keeps the oxygen concentration low. On the other hand, the much weaker circulation represented by the solutions (30–32) can involve direct flow from the crucible bottom to the crystal face in the inner core, so that there is no reduction of the oxygen concentration on these streamlines because of evaporation from the free surface. Therefore, the effect of the weaker circulation on the oxygen concentration in the crystal may be at least as great as that of the stronger circulation.

The free-shear-layer variables with primes or double primes represent circulation with $O(M^{-\frac{1}{2}})$ or $O(M^{-1})$ flow rates, respectively, so that their contributions to the flow inside the free shear layer are negligible compared to those of the variables without primes. However, these free-shear-layer perturbations are important because of their relationships to the circulation outside the free shear layer. There are certain assumptions about the free-shear-layer solutions which are implicit in the solutions presented in §4. The first assumption is that the $O(1)$ and $O(M^{-\frac{1}{2}})$ flows inside the free shear layer do not produce comparable flows in the adjacent cores. The solutions (43–45) demonstrate that this is true for the $O(1)$ flow. We can draw the same conclusion about the $O(M^{-\frac{1}{2}})$ flow without finding its solution. The equations (34) and the boundary conditions (35, 36), with primes added, as well as the conditions (37c, 38b, 39c), constitute a well-posed boundary-value problem for the variables with primes. The flow is driven by the $O(M^{-\frac{1}{2}})$ term in the centrifugal force represented by H_1', by the effects of the curvature of the free shear layer represented by H_2' and H_3', and by the fact that the bounding streamline must follow the deflected free surface for $\zeta > 0$ represented by the condition (39c). When we introduce the solutions (25), and we manipulate (34), we can show that the solutions can in fact satisfy the boundary conditions (35, 36), which implicitly assume that there are no $O(M^{-\frac{1}{2}})$ perturbations in the inner and outer cores. Therefore, the free-shear-layer variables with primes represent a meridional circulation with an $O(M^{-\frac{1}{2}})$ flow rate which is also entirely contained within the free shear layer.

The equations (34) and the boundary conditions (35, 36), with double primes added, as well as the conditions (37a, 38c, 39a) also represent a well-posed boundary-value problem, now for the variables with double primes. The solutions represent a circulation with an $O(M^{-1})$ flow rate, but this circulation is not confined to the free shear layer. Indeed, figures 7–9 assume that the free shear layer provides certain $O(M^{-1})$ flows between the Hartmann layers and the inner core in each case. Again we can show that the solutions of (34) can satisfy the boundary conditions (35–39), so that we need only show that the boundary-value problem implies precisely the $O(M^{-1})$ flows across the boundaries of the free shear layer, which are assumed in figures 7–9.

The integral of the boundary condition (37a) from $\zeta = -\infty$ to $\zeta = \infty$, and the boundary conditions (24a, d, 35, 36) show that

$$\int_{-\infty}^{\infty} v_{zf}''(\zeta, 0)\,\mathrm{d}\zeta = Q_c(a), \tag{48}$$

where Q_c is given by the expression (30a). The solution for the $O(1)$ radial velocity in the intersection region at $z = 0$ shows that this region accepts a flow of $Q_c(a)$ from the Hartmann layer at $z = 0$, $r = a$, and delivers the same flow to the free shear layer, as indicated by (48). The boundary condition (36) with H_5'' indicates that the free shear layer provides the assumed $O(M^{-1})$ flow to or from the inner core.

To understand the $O(M^{-1})$ flow, $Q_s(a)$, from the Hartmann layer on the crystal face, through the intersection region and into the free shear layer, we must consider the structure of the intersection region at the crystal edge. This region actually consists of two intersection regions: one adjacent to the free surface for $\zeta > 0$ which satisfies the boundary conditions (4), and the other adjacent to the crystal face for $\zeta < 0$ which satisfies the boundary conditions (5, 7c, d). These two intersection regions are separated by a corner region at the crystal edge, which has $O(M^{-1}) \times O(M^{-1})$ dimensions in meridional planes and which matches any differences in the structures of the two intersection regions. There is no corner region at $z = 0$ because there is no physical discontinuity along the crucible bottom at $r = a$. The $O(1)$ and $O(M^{-\frac{1}{2}})$ tangential velocities, v_θ and v_t, are continuous through the intersection region on the free surface, so that this region makes no $O(M^{-1})$ or $O(M^{-\frac{3}{2}})$ adjustments to the tangential flows in the free shear layer here, i.e. its displacement thickness is zero to these orders. In the intersection region on the crystal face, there are two $O(M^{-1})$ adjustments to the radial flow in the free shear layer at $z = b$. First, there is an exponential variation from $v_{rf}(\zeta, b)$ at $Z' = -\infty$ to zero at $Z' = 0$, so that there is a boundary-layer flow deficiency. Since there is no corresponding deficiency for $\zeta > 0$, the $O(M^{-1})$ flow deficiency corresponding to $v_{rf}(0, b)$, must enter the corner region from the free shear layer, flow radially inward into the intersection region on the crystal face and then feed gradually back into the free shear layer as $v_{rf}(\zeta, b) \rightarrow 0$, as $\zeta \rightarrow -\infty$. The free shear layer sees a mass sink at $\zeta = 0$, $z = b$. This $O(M^{-1})$ circulation due to the boundary-layer deficiency associated with the no-slip condition (5a) is confined to the free shear layer, corner region and intersection region on the crystal face.

The second $O(M^{-1})$ radial flow in this intersection region is that driven by the centrifugal force associated with the exponential variation of v_θ from $v_{\theta i}(a)$ at $Z' = -\infty$ to ϵa at $Z' = 0$. This part of the $O(1)$ radial velocity in this region is given by the expression (28b) evaluated at $r = a$, which corresponds to an $O(M^{-1})$ radial flow of $Q_s(a)$. The flow $Q_c(a)$ is fed into the free shear layer from the bottom intersection region over their entire $O(M^{-\frac{1}{2}})$ radial dimension because $v_{\theta f}(\zeta, 0)$ varies gradually from $v_{\theta i}(a)$ to a. However, the $Q_s(a)$ from the top Hartmann layer flows through the top intersection region to the corner region with none flowing into the free shear layer from the intersection region, because $v_{\theta f}(\zeta, b) = v_{\theta i}(a)$ for all $\zeta < 0$. Since there is no corresponding flow in the intersection region on the free surface, the flow $Q_s(a)$ enters the free shear layer from the corner region and appears to the free shear layer as a mass source or sink at $\zeta = 0$, $z = b$.

The free shear layer must accept the appropriate mass sources and sinks at $\zeta = 0$, $z = b$. When the solutions (40, 43–45) are introduced into the term $\partial^2 v_{rf}/\partial\zeta^2$ in H_1'' and into the term $\partial^2 v_{zf}/\partial z^2$ in H_3'', these inhomogeneous terms are singular at $\zeta = 0$, $z = b$, while all the other terms in H_1'', H_2'' and H_3'' are well behaved here. The solutions of (34), which accommodate these singular inhomogeneous terms, are themselves singular at $\zeta = 0$, $z = b$, and these singularities involve exactly the flow rates into or out of this point needed for $Q_s(a)$ and for the flow deficiency associated with $v_{rf}(0, b)$. Therefore, the free-shear-layer variables with double primes do complete the $O(M^{-1})$ flow circuit as assumed in figures 7–9. These variables are able to accommodate the appropriate mass source or sink at the crystal edge because the $O(1)$ free-shear-layer flow solution involves singularities in the viscous terms which enter the $O(M^{-1})$ flow problem to provide just the correct singular driving terms. Therefore, if there were no $O(1)$ circulation inside the free shear layer, then this layer would not be able to complete the $O(M^{-1})$ flow circuit as assumed. The structure of corner regions and how they match singularities in the free-shear- and vertical-wall-layer solutions are discussed by Cook, Ludford & Walker (1972).

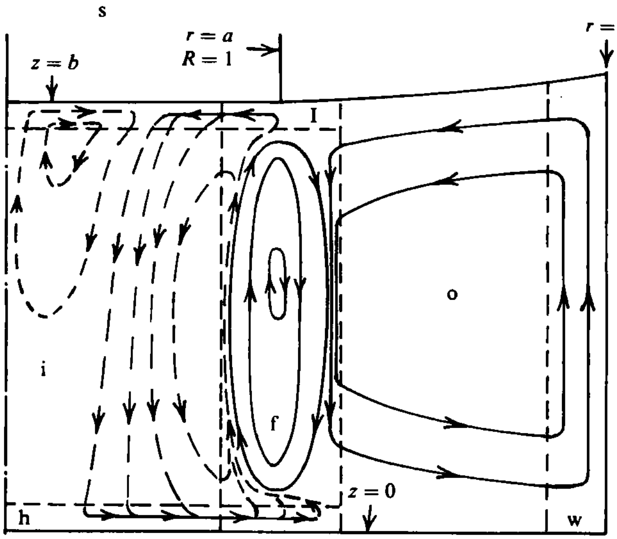

FIGURE 12. Sketch of streamlines in meridional planes with superposition of the circulations in figures 9 and 11, and a buoyancy-driven circulation which is blocked by the free shear layer. Dashed lines represent much weaker circulations than solid ones.

6. Discussion

When we superpose the free shear layer's axial contributions to the $O(M^{-1})$ circulations in figures 7–9 and its own $O(1)$ internal circulation, the latter overwhelms the former. Therefore, the streamlines in the free shear layer always resemble those in figure 11, plus an additional streamline between the top and bottom, either to the right of the others, i.e. near the edge with the outer core, or to the left of the others, i.e. near the edge with the inner core. If the axial free-shear-layer flow in one of the figures 7–9 is upward, then the free-shear-layer circulation sweeps it towards the inner core, and the additional streamline is on the left. If this axial flow is downward, then the free-shear-layer circulation sweeps it towards the outer core, and the added streamline is on the right. If this axial flow is downward and there is flow from the free shear layer into the inner core, as in figure 7(*e*), then the flow from the top Hartmann layer enters the free shear layer and flows to the bottom near the edge with the outer core. At the bottom, this flow splits and part enters the bottom Hartmann layer for $r < a$, while the rest flows back up the free shear layer, but now near the edge with the inner core, and feeds into the inner core at various elevations.

If the crystal and the crucible have the same angular velocities (iso-rotation, $\epsilon = 1$), then the only meridional circulation is that due to buoyancy. This circulation consists of an axial upward flow inside the vertical wall layer at $r = 1$, radial inward or outward flow near the free surface or near the crucible bottom, respectively, and an axial downward flow under the relatively cold crystal face. This circulation pattern is evident in the figures 5(*b, c*) and 6(*b–d*) presented by Langlois & Lee (1983) for the meridional circulations with no rotations. This circulation involves a dimensionless flow rate which is $O(v_{\mathrm{bc}})$, where $v_{\mathrm{bc}} = 0.052$. Since v_{bc} is independent of B, the actual flow rates due to buoyancy decrease as B^{-2}. In figures 6(*c, d*) presented by Langlois & Lee (1983), there are nine and three streamlines for $B = 0.1$ T and $B = 0.2$ T, respectively. The flow pattern also changes as B increases because the contribution of convection, relative to that of conduction, decreases as the Péclet number decreases.

When we introduce a differential rotation between the crucible and the crystal ($\epsilon \neq 1$), the temperature distribution is changed because of the thermal convection with the meridional motion due to the centrifugal force. However, the basic flow pattern for the buoyancy-driven flow remains qualitatively the same. When we superpose the circulations due to buoyancy and centrifugal force, the resultant flow depends on the relationship between the radial velocities in the free shear layer due to the centrifugal force and the radial velocities due to buoyancy at $r = a$. These velocities are in opposite directions both near the crystal edge and near the crucible bottom. If the centrifugal-force velocities are larger than the buoyancy ones, then the free shear layer blocks the buoyancy circulation, so that it cannot penetrate into the inner core. If the centrifugal-force velocities are smaller, then the free shear layer deflects the buoyancy streamlines towards $z = \frac{1}{2}b$ at $r = a$. Some of these streamlines that were near $z = \frac{1}{2}b$ for $r > a$ close at $r = a$, but the streamlines that were near the free surface and the bottom for $r > a$ pass through the free shear layer and return to their original elevations once inside the inner core. The effect of this buoyancy-flow penetration into the inner core is to bring fluid, which is low in oxygen because it has travelled along the free surface, into the part of the inner core near the crystal edge. This flow does not penetrate far beyond the crystal edge because the isothermal crystal face quickly cools it, so that it sinks towards the bottom. The result may be an unacceptable radial variation of oxygen concentration in the crystal. Therefore, it appears to be desirable to ensure that the centrifugal-force circulation is sufficiently strong to block the buoyancy-driven circulation at $r = a$. This could be achieved by increasing the magnitude of $(1-\epsilon)$ until blockage occurs. However, ϵ is chosen in order to achieve a desirable flow pattern in the inner core, e.g. $\epsilon = -0.38$ for figure 9. For a fixed, non-zero value of $(1-\epsilon)$, the centrifugal force is increased relative to the buoyancy force by increasing Ω, i.e. by increasing the rotation speeds of both the crystal and crucible while keeping the ratio of their angular velocities constant. The effect of increasing Ω is to decrease N and v_{bc}, and to increase Pe. If we superpose the circulations in figures 9 and 11, and a buoyancy-driven circulation which is blocked by the free shear layer, we obtain the sketch of streamlines given in figure 12.

Numerical solutions of the heat equation and the specific details of the buoyancy-driven flows will be presented in a future paper. The specific values of v_{rf} from the free-shear-layer solutions (40, 43–45) are not important here because they overwhelm the circulations driven by the Hartmann layer and inner-core centrifugal pumping. On the other hand, these values of v_{rf} are very important when the buoyancy circulation is added because they must be larger than the buoyancy v_r at $r = a$ in order to block the buoyancy-driven circulation. Therefore, graphs of v_{rf} from the solutions (40, 43–45) will be presented in a future paper along with the solutions for the buoyancy-driven circulation.

The weak electrical conductivity of the crystal plays a key role in determining the present solutions. For the present configuration with an axial, uniform magnetic field, the electrical generator in the problem is the axial variation of the azimuthal velocity in the column of fluid beneath the crystal. The azimuthal velocity across the axial magnetic field produces a radial voltage difference. When this velocity varies with z, as it must for any differential rotation ($\epsilon \neq 1$), then the voltage differences appear as radial batteries with different strengths at different elevations. The imbalance between batteries drives a meridional circulation of electrical current, and the crystal is one of the electrical resistors in the circuit for this current.

For a Czochralski crystal grower with a steady, uniform, transverse magnetic field, the weak electrical conductivity of the crystal plays an even more important role.

With a transverse field, the bulk of the fluid has no $O(1)$ azimuthal velocity. The fluid is held by the field lines, and only the fluid in the Hartmann layers on the vertical crucible wall and in the boundary layers on the crucible bottom and on the crystal face have an $O(1)$ azimuthal velocity which equals r at the crucible and ϵr at the crystal face. There is an $O(M^{-1})$ horizontal velocity along magnetic field lines from one side of the crucible to the other, which is driven by the azimuthal variation of the Hartmann-layer structure.

If we consider a horizontal section through a crystal rotating in a uniform, transverse magnetic field, the halves of the section on opposite sides of the diameter perpendicular to the magnetic field are moving across the magnetic field lines in opposite directions. Therefore, the axial induced electric field, $\epsilon r\hat{\boldsymbol{\theta}} \times \boldsymbol{B}$, has opposite signs on opposite sides of this diameter. This electric field drives electric currents up and down the crystal on opposite sides of this diameter. At the crystal face, these currents enter the melt and produce an EM body force in the melt near the crystal face. With a transverse magnetic field, the crystal is the electrical generator, and the melt is the resistor in the electrical circuit. How the electrical circuit is completed through the melt and how the melt responds to the rèsultant EM body force are the keys to the flow in a Czochralski crucible with a transverse field. For the problem with a transverse field, the spherical shape of the crucible bottom and the concave shape of the crystal face are very important. If these surfaces were plane, the boundary layers on them would have $O(M^{-\frac{1}{2}})$ thicknesses, but the actual surfaces have Hartmann layers with $O(M^{-1})$ thicknesses. Solutions for this problem will be presented in a future paper.

In our discussion of the present results, we have treated the ratio of resistances γ as a function of magnetic field strength B, and have taken the electrical conductivity of the crystal as a constant, namely $\sigma_s = 3.16 \times 10^4$ mho/m. In reality, σ_s is a function of the concentrations of dopants and impurities in the crystal. Some impurities, such as aluminium, have particularly strong effects on the crystal conductivity. An increase in σ_s merely increases γ as an increase in B would. To double γ, we can double B or σ_s or the crystal radius aL, since $\gamma = \sigma_s BaL(\sigma\rho\nu)^{-\frac{1}{2}}$. Actually, σ_s and B cannot be treated independently. Any change in the magnetic field strength changes the mass transport of dopants and impurities to the crystal. An increase in B may increase or decrease σ_s, so the variation of γ with B is more complex than our simplified discussion implies.

This research was supported by the US National Science Foundation under Grant CPE-8108952 and by the Monsanto Electronic Materials Company.

REFERENCES

Cook, L. P., Ludford, G. S. S. & Walker, J. S. 1972 Corner regions in the asymptotic solution of $\epsilon\nabla^2 u = \partial u/\partial y$ with reference to MHD duct flow. *Proc. Camb. Phil. Soc.* **72**, 117–122.

Hays, P. R. & Walker, J. S. 1984 Liquid-metal MHD open-channel flows. *Trans. ASME* E: *J. Appl. Mech.* **106**, 13–18.

Hoshikawa, K. 1982 Czochralski silicon crystal growth in the vertical magnetic field. *Jpn J. Appl. Phys.* **21** (9), L545–L547.

Kakutani, T. 1962 Hydromagnetic flow due to a rotating disk. *J. Phys. Soc. Japan* **17**, 1496–1506.

Kim, K. M., Schwuttke, G. H. & Smetana, P. 1981 Apparatus for Czochralski silicon crystal growth through axial magnetic field fluid flow damping. *IBM Technical Disclosure Bulletin* **24** (7 A), 3376–3377.

Langlois, W. E. 1981 Convection in Czochralski growth melts. *Physico Chem. Hydrodyn.* **2** (4), 245–261.

LANGLOIS, W. E. & LEE, K. J. 1983 Digital simulation of magnetic Czochralski flow under various laboratory conditions for silicon growth. *IBM J.* **27** (3), 281–284.

LANGLOIS, W. E. & WALKER, J. S. 1982 Czochralski crystal growth in an axial magnetic field. *Computational and Asymptotic Methods for Boundary and Interior Layers*, Proceedings of the BAIL II Conference, pp. 299–304.

LEE, K. J., LANGLOIS, W. E. & KIM, K. M. 1984 Digital simulation of oxygen transfer and oxygen segregation in magnetic Czochralski growth of silicon. *Physico Chem. Hydrodyn.* **5** (2), 135–141.

PETRYKOWSKI, J. C. & WALKER, J. S. 1984 Liquid-metal flow in a rectangular duct with a strong non-uniform magnetic field. *J. Fluid Mech.* **139**, 309–324.

ZULEHNER, W. 1983 Czochralski growth of silicon. *J. Crystal Growth* **65**, 189–213.